AIAA'87

AIAA-87-0415

# VISCOUS TRANSONIC AIRFOIL WORKSHOP RESULTS USING ARC2D

Catherine M. Maksymiuk
and Thomas H. Pulliam
NASA Ames Research Center, Moffett Field, CA

**AIAA 25th Aerospace Sciences Meeting**
January 12-15, 1987/Reno, Nevada

For permission to copy or republish, contact the American Institute of Aeronautics and Astronautics
1633 Broadway, New York, NY 10019

# Viscous Transonic Airfoil Workshop Results Using ARC2D

CATHERINE M. MAKSYMIUK[1]
AND
THOMAS H. PULLIAM[2]

NASA Ames Research Center
Moffett Field, CA. 94035

ABSTRACT. Computations have been performed in response to the Viscous Transonic Airfoil Workshop associated with the AIAA 25th Aerospace Sciences Meeting (January 1987). The purpose of the workshop is to establish the capabilities of various methods for computing viscous flowfields for a range of conditions and geometries. The results of the test cases will demonstrate the capabilities of the methods in predicting both aerodynamic trends and flowfield details. ARC2D, a well-established Navier-Stokes code, was used to compute the flowfields for the designated airfoils, Mach numbers, angles of attack and other specifications of the Workshop committee.

## INTRODUCTION

In response to the Viscous Transonic Airfoil Workshop which is associated with the AIAA $25^{th}$ Aerospace Sciences Meeting, a series of two-dimensional airfoil Navier-Stokes computations are presented. The purpose of the workshop is to establish the capabilities of various methods for computing viscous flowfields for a range of conditions and geometries. Detailed specifications were obtained from the Workshop Committee and all required and suggested computations are presented. The computations were performed using the Navier-Stokes code ARC2D, which is based on the implicit approximate factorization algorithm of Beam and Warming [1]. The code was originally developed by Steger [2] and has been steadily improved, enhanced and modified over the past 5 years, Ref. [3], [4], and [5].

The algorithm is an implicit approximate factorization finite difference scheme which can be either first or second order accurate in time. Local time linearizations are applied to the nonlinear terms and an approximate factorization of the two-dimensional implicit operator is used to produce locally one-dimensional operators. This results in block tridiagonal matrices, which are easy to solve. The spatial

[1]Research Scientist. Computational Physics Section, CFD Branch. Member AIAA
[2]Research Scientist. Head Computational Physics Section, CFD Branch. Member AIAA

This paper is declared a work of the U.S. Government and is not subject to copyright protection in the United States.

derivative terms are approximated with second order central differences. Explicit and implicit artificial dissipation terms are added to achieve nonlinear stability. A spatially variable time step is used to accelerate convergence for steady–state calculations. A diagonal form of the algorithm is also employed, which produces a computationally efficient modification of the standard algorithm where the diagonalization results in scalar tridiagonal or pentadiagonal operators in place of the block operators. This diagonal form of the algorithm produces a robust, rapid and versatile scheme for steady state calculations. The code can perform either in the accelerated steady–state mode or in a time accurate mode.

The Baldwin–Lomax turbulence model is used in all the following computations. It is an algebraic model, and is described in Reference 6. The model has been used in computing solutions for a wide variety of conditions, and has been found to be acceptably accurate.

## II. Viscous Transonic Airfoil Workshop Specifications

Results for three airfoil profiles: A) NACA 0012, B) RAE 2822 and C) a supercritical airfoil due to R. T. Jones (Jones Airfoil) are presented. Airfoil coordinates were provided and a series of general "C" meshes generated with a hyperbolic solver, Ref. [7], were used for the flowfield computations. Parameters for the hyberbolic solver include total number of grid points (369 x 65 for most of the cases presented here), number of points on the upper and lower surfaces (152 on each surface) and in the wake (33), normal spacing at the body (.00002), clustering along the surface (spacing is .001 at the leading edge and .002 at the trailing edge, and outer boundary position (25 chords for most cases). A view of the mesh used in the NACA 0012 cases is shown in Figure 1.

The workshop specifications include required cases, suggested cases and low priority cases. Mach numbers, angles of attack, Reynolds numbers, and transition points are specified, and various quantities, such as $C_p$ (coefficient of pressure), boundary layer profiles, and $C_f$ (skin friction coefficient), are to be plotted. Curves of $C_l$ ( coefficient of lift) vs. $\alpha$ (angle of attack), $C_l$ vs. $C_d$ (coefficient of drag) and $C_d$ vs. $M_\infty$ (Mach number) are requested. Grid refinement and outer boundary location studies are also suggested. All of the required and suggested data is presented here. Plots are shown to the specifications of the committee; where the requested scaling seemed inappropriate, additional plots are given to present the features accurately. In the solution requirements document, each case is designated as: A) NACA 0012, B) RAE 2822 and C) Jones airfoil, numbered (e.g. A(1)) for specific cases. This notation shall be followed here.

## III. RESULTS

### A. NACA 0012 Studies

Computations were performed for the NACA 0012 airfoil at three specified conditions and various lift, drag and Mach number curves were obtained. The grid for these computations is described above and shown in Figure 1. For all these cases, the Reynolds number was 9 million. Transition was fixed at 5% of chord on both the upper and lower surfaces. Geometric angles of attack from the experimental data of Harris [Ref. 9] were specified; corrections suggested by Harris [9] were used in the computations.

**A(1)** $C_p$ **vs.** $x/c$ – $M_\infty = 0.7, \alpha = 1.86°$, **Corrected** $\alpha_c = 1.49°$.

The computed coefficient of pressure data for this case is compared with the experimental data of Harris [9] in Figure 2. The results agree very well with experiment except along the upper surface between 10% and 20% of chord. The numerical solution has an overexpansion and weak shock in this region, while the experiment shows a smooth compression. Mach contours are shown in Figure 3; a small region of supersonic flow can be seen. Transition is evident in the numerical solution; there is a small glitch on the pressure coefficient plot at 5% of chord. The experiment shows a similar glitch slightly further back and of larger magnitude. The disparity in transition possibly gives rise to the shock/compression disparity.

**A(2)** $C_p$ **vs.** $x/c$ – $M_\infty = 0.55, \alpha = 9.86°$, **Corrected** $\alpha_c = 8.34°$.

Results for the second case are shown in Figure 4. Again the results compare very well with experiment, except in the shock region. ARC2D produces a sharper shock than is found in the experiment. The discrepancy is most likely due to an inaccuracy in the shock/boundary layer interaction. This is more evident in the next case.

**A(3)** $C_p$ **vs.** $x/c$ – $M_\infty = 0.799, \alpha = 2.86°$, **Corrected** $\alpha_c = 2.26$.

As shown in Fig. 5, the greatest discrepancy between computation and experiment is found in this case. Here the computation matches experimental data fairly well, except that the shock location is computed about 10% of chord further back than the experiment. Shadowgraph pictures from McDevitt and Okuno, Ref. 8, show results from a similar case ($M_\infty = 0.8, \alpha = 2.5°, Re = 6 \times 10^6$). This experiment has a lambda shock with the strongest part of the shock located at about 55% of chord a short distance off of the surface. Near the surface the shock curves in to about 45% of chord. A relatively thick boundary layer can be seen just after the shock. Both shock curvature and boundary layer thickening can be observed in the numerical solution, but they are not as pronounced as in the experiment. This is probably attributable to the turbulence model. Since the effects of turbulence

modeling have not been examined in detail for these results, we will not speculate further on this discrepancy as far as turbulence modeling is concerned.

One possible source of error which we can examine is the effect of artificial dissipation. The dissipation coefficients were halved and doubled relative to the baseline case, and the resulting pressure coefficient distributions are shown in Figure 6. The shock position is only slightly altered by these variations.

**A(4)** $C_l$ **vs.** $\alpha$ - $M_\infty = 0.7$, $\alpha = 1°, 3°, 5°, 6°, 7°$

**A(5)** $C_l$ **vs.** $C_d$ – $M_\infty = 0.7$, $\alpha = 0°, 1°, 3°, 5°, 6°, 7°$

Studies of the variation of lift coefficient with angle of attack and with drag coefficient at a free–stream Mach number of 0.7 were undertaken. The results are shown in Figures 7–9. For the $C_l$ - $\alpha$ study, the experimental data is plotted at geometric and corrected angles of attack. The computed results agree well with experimental data at corrected angles of attack, up to about 5.0°. At 6° and 7°, the code produced unsteady results. The solution is periodic in both cases, and the variation of lift with time is plotted in Figure 8. Maximum lift coefficient is approximately 0.8, after which the flow becomes unsteady. The drag polar (Figure 9) is also calculated reasonably well in comparison to experimental data.

**A(6)** $C_d$ **vs.** $M_\infty$ – $\alpha = 0°$, $M_\infty = 0.5, 0.6, 0.7, 0.8, 0.9, 1.0, 1.1$

A plot of the computed results is shown in Figure 10. The code predicts the occurrence of drag rise at a Mach number of approximately 0.8 and a maximum drag coefficient of 0.115 at 0.9 Mach number. There was no experimental data available in Ref. [9] for a direct comparison, but some related data indicates that the prediction of drag divergence is accurate.

**A(7)** $C_l$ **vs. del,** $M_\infty = 0.7, \alpha = 1.49°$

**A(8)** $C_d$ **vs. del,** $M_\infty = 0.7, \alpha = 1.49°$

Results of a grid refinement study are given in Figures 11 and 12. Aerodynamic coefficients $C_l$ and $C_d$ are plotted against del, the inverse of the number of upper surface grid points. Six grids were used in the study: 369 x 65, 321 x 58, 257 x 46, 193 x 35, 161 x 29, 129 x 23; the ratio of points in the two directions (5.5 - 5.6), distance to the outer boundary (25 chords), and number of points in the wake (33) were kept constant. Both plots show that the coefficients approach an asymtotic limit as the grid is refined. There is considerably more variation in the drag coefficient, probably because it is more sensitive to changes in stretching in the normal direction. Since each grid is different, the normal spacing varies and the drag coefficient is affected.

**A(9)** $C_l$ **vs. R,** $M_\infty = 0.7, \alpha = 1.49^\circ$

**A(10)** $C_d$ **vs. R,** $M_\infty = 0.7, \alpha = 1.49^\circ$

The influence of the outer boundary position on aerodynamic coefficients was studied. Five grids were used, with dimensions of 257 x 81, 257 x 79, 257 x 77, 257 x 73, and 257 x 66. The base grid with the outer boundary at 50 chords was obtained as described above. Successive grids were obtained by removing outer rings to insure that the spatial distribution was the same for all grids. As shown in Figures 13 and 14, the lift and drag coefficients are essentially constant with respect to outer bounday position.

## B. RAE 2822 Airfoil Studies

Two specific cases were computed for the RAE 2822 Airfoil. In both cases, the Reynolds number was $6.5 \times 10^6$, and transition points were located at 0.03 chords. Angle of attack corrections were obtained by attempting to match lift to the experimental data of Cook, McDonald, and Firmin [Ref. 10]. The grid had a resolution of 369 x 65 points and is shown in Figure 15. All numerical results displayed in Figures 16–26 were computed using the corrected angle of attack; corresponding experimental data was obtained from Ref. 10. Data for the boundary layer plots was published as $u/u_p$ where $u_p$ is the velocity at the edge of the boundary layer. These values were multiplied by the computed $u_p/u_\infty$, so they could be compared directly with the numerical results.

$M_\infty = 0.725, \alpha = 2.92^\circ$, **Corrected** $\alpha_c = 2.30^\circ$.

**B(1)** $C_p$ **vs.** $x/c$

**B(2)** $\delta^*/c$ **vs.** $x/c$

**B(3)** $C_f$ **vs.** $x/c$

**B(4)** $y/c$ **vs.** $u/u_\infty$, $x/c = 0.319$

**B(5)** $y/c$ **vs.** $u/u_\infty$, $x/c = 0.95$

Figure 16 shows the pressure coefficient along the airfoil surface. Agreement with experimental data is quite satisfactory, although the shock location is computed slightly forward of the experimental location and the compression at the leading edge is not quite strong enough. These discrepancies are opposite to errors that were found in the NACA 0012 cases, where the shock location was too far back and the leading edge compression was too strong. In this case, lack of agreement between experiment and computations is probably due more to an improper angle of attack correction than to any turbulence model considerations.

A plot of momentum thickness ($\delta^*/c$) along the upper surface is given in Figure 17. The computation of skin friction coefficient is shown in Figure 18. Near the leading edge, the numerical result shows a large oscillation. This reflects the dependence of the skin friction coefficient on transition.

Boundary layer profiles are plotted in Figures 19 and 20. Fig. 19b is plotted on an enlarged scale to show detail; the agreement with experimental data is satisfactory at 31.9% chord. The computed profile exhibits less agreement at 95% chord; it has a generally higher velocity in the middle of the boundary layer. This is probably a failing of the turbulence model, similar to the cases where the boundary layer was not as thick and separation was not as severe as the experiments show. The conditions of this case are more benign, so the turbulence model does not fail as radically or affect the solution as much as in the cases described above.

$M_\infty = 0.75, \alpha = 3.19°$, **Corrected** $\alpha_c = 2.92°$.

**B(6)** $C_p$ **vs.** $x/c$
**B(7)** $\delta^*/c$ **vs.** $x/c$
**B(8)** $C_f$ **vs.** $x/c$
**B(9)** $y/c$ **vs.** $u/u_\infty$, $x/c = 0.319$
**B(10)** $y/c$ **vs.** $u/u_\infty$, $x/c = 0.95$
**B(11) sonic line**

At a higher angle of attack and Mach number, this case has more severe conditions than the above case, and in general the numerical solution is less satisfactory. Figure 21 shows the pressure coefficient. The shock is computed too far back and the leading edge expansion and compression is not captured very accurately. The latter problem is attributable to the angle of attack correction, but the former is more dependent on the turbulence model and reflects the same problems as in case A(3) above.

As shown in the plot of momentum thickness (Figure 22) the numerical solution produces a larger $\delta^*$ than the experiment. The computed shock is stronger than in the experiment; this might give rise to a thicker boundary layer near the trailing edge. The computed skin friction (Figure 23) shows some error in this region, but in general it matches the experimental data more closely than in the other RAE case. Boundary layer profiles (Figures 24 and 25) show that the experimental solution has some tendency toward separation while the numerical result displays no such character. This is a manifestation of the shock/boundary layer problem discussed in case A(3).

A plot of the sonic (Mach = 1) line is given in Figure 26.

### C. Jones Airfoil Studies.

The Jones airfoil is a supercritical airfoil designed by R. T. Jones. No experimental data is available for comparison in these cases. All the cases had a Reynolds number of 9 million and transition fixed at the leading edge. The grid is shown in Figure 27.

**C(1)** $C_l$ **vs.** $\alpha$ – $M_\infty = 0.7$, $\alpha = 0°, 1°, 3°, 5°, 6°, 7°$

**C(2)** $C_l$ **vs.** $C_d$ – $M_\infty = 0.7$, $\alpha = 0°, 1°, 3°, 5°, 6°, 7°$

Figures 28–30 show the behavior of aerodynamic coefficients for a range of angles of attack. Lift coefficient (Fig. 28) displays a typical linear relationship through an angle of attack of 5°. Unsteady results were obtained for angles of 6° and 7°. The unsteady solutions are very similar to the unsteady results of the NACA 0012. Figure 29 shows the periodicity of lift coefficients through two cycles. $C_{l_{max}}$ can be estimated at approximately 0.96. The drag polar (Fig. 30) is also typical: some profile drag exists at low levels of lift, then drag increases radically as lift increases.

**C(3)** $C_d$ **vs.** $M_\infty$ – $\alpha = 0°$, $M_\infty = 0.5, 0.6, 0.7, 0.8, 0.9, 1.0, 1.1$

The variation of drag coefficient with Mach number is presented in Figure 31. Drag rise is seen to occur at about Mach 0.75, and $C_{d_{max}}$ is approximately 0.11. The case with $M_\infty = 0.9$ was especially difficult to run. The time accurate option was used, but the results are not typical of truly unsteady cases, i.e. there was no periodicity. A shock formed on the upper surface very near the trailing edge, and moved back and forth very slightly.

$M_\infty = 0.75, \alpha = 2.0°$.

**C(4)** $C_p$ **vs.** $x/c$
**C(5)** $\delta^*/c$ **vs.** $x/c$
**C(6)** $C_f$ **vs.** $x/c$
**C(7)** $y/c$ **vs.** $u/u_\infty$, $x/c = 0.6$
**C(8)** $y/c$ **vs.** $u/u_\infty$, $x/c = 0.9$

This supercritical case has a shock located at about 45% of chord. The pressure coefficient on the surface is given in Figure 32. Figure 33 shows the momentum thickness. Near the trailing edge, the boundary layer increases, and relatively sharp slopes are found on the plot. This is because momentum thickness is computed using the edge of the boundary layer. When that reference changes, the momentum thickness may change sharply. Skin friction coefficient is plotted in Figure 34. Boundary layers at 60% and 90% of chord are shown in Figures 35 and 36. The profiles look smooth and turbulent.

$M_\infty = 0.85, \alpha = 2.0°$.

**C(9)** $C_p$ **vs.** $x/c$
**C(10)** $\delta^*/c$ **vs.** $x/c$
**C(11)** $C_f$ **vs.** $x/c$
**C(12)** $y/c$ **vs.** $u/u_\infty$, $x/c = 0.6$
**C(13)** $y/c$ **vs.** $u/u_\infty$, $x/c = 0.9$

This case demonstates the capability of ARC2D with regard to computing separation. The pressure coefficient on the surface is given in Figure 37. Figure 38 shows

the momentum thickness. The dependence of this quantity on a reference is shown even more strongly here. The separated region forms a "bubble," but the boundary layer thickness within the bubble may change. A large oscillation in momentum thickness is evident in Fig. 38. Skin friction coefficient is plotted in Figure 39. Its value is quite low in the separation zone. Boundary layers at 60% and 90% of chord are shown in Figures 40 and 41. The latter plot clearly shows a small separation region.

### D. Additional Data.

Data describing the computational characteristics was requested in the workshop specifications. Table 1 shows various characteristic of the require cases. The minimum cpu time needed for any of the required cases was 925 seconds, corresponding to 2000 iterations. Most of the cases were converged at this point. Among the required steady-state cases, maximum cpu time was used for the NACA 0012 at $M_\infty = 0.9$ and $\alpha = 0°$. This case was run for 2254 seconds (4500 iterations); however, the aerodynamic coefficients were constant after 1986 seconds (4000 iterations). Unsteady cases required much more cpu time and were run until periodicity was firmly established. Among all the cases, the Jones airfoil supercritical separated cases required the most cpu time, 3700 seconds for 7000 iterations.

Grids for the required computations had a resolution of 369 x 65 points. The outer boundary located at about 25 chords. Yplus values one grid spacing from the wall for case A(1) were 8.9926 at 20% chord, 8.4661 at 50% chord, and 7.5836 at 80% chord.

The CRAY X-MP48 at NASA-Ames Research Center was used. ARC2D is highly vectorized; the ratio of scalar cpu time to vectorized cpu time is about 0.05. The code performs on the X-MP at 70 MFLOPS. The required cases used 1864 kwords of main memory.

| TABLE 1 Data for required cases | | | | | | |
|---|---|---|---|---|---|---|
| Case | $M_\infty$ | $\alpha$ | $C_l$ | $C_d$ | iterations | conv. criteria |
| A(2) | .55 | 8.34 | .988 | .0362 | 2000 | $6.5 \times 10^{-5}$ |
| A(3) | .799 | 2.26 | .472 | .0445 | 3000 | $2.6 \times 10^{-6}$ |
| A(4) | .7 | 0.0 | 0.0 | .0080 | 2000 | $3.8 \times 10^{-4}$ |
| | .7 | 1.0 | .169 | .0082 | 2000 | $6.4 \times 10^{-5}$ |
| | .7 | 3.0 | .503 | .0144 | 2000 | $4.4 \times 10^{-5}$ |
| | .7 | 5.0 | .763 | .0431 | 2000 | $2.7 \times 10^{-5}$ |
| | .7 | 6.0 | unsteady | | | |
| | .7 | 7.0 | unsteady | | | |
| A(6) | .5 | 0.0 | 0.0 | .0075 | 3000 | $1.8 \times 10^{-5}$ |
| | .6 | 0.0 | 0.0 | .0077 | 3000 | $5.3 \times 10^{-5}$ |
| | .8 | 0.0 | 0.0 | .0159 | 3500 | $6.2 \times 10^{-4}$ |
| | .9 | 0.0 | 0.0 | .1150 | 4000 | $3.7 \times 10^{-4}$ |
| | 1.0 | 0.0 | 0.0 | .1097 | 2000 | $4.1 \times 10^{-4}$ |
| | 1.1 | 0.0 | 0.0 | .1027 | 2000 | $2.2 \times 10^{-3}$ |
| B(6) | .75 | 2.72 | .838 | .0289 | 2000 | $1.0 \times 10^{-6}$ |
| C(1) | .75 | 2.0 | .558 | .0178 | 2000 | $2.7 \times 10^{-4}$ |

## Remarks

The results of these cases indicate that ARC2D can adequately predict aerodynamic trends. Good results were obtained for Mach numbers ranging from 0.5 to 1.1 at zero angle of attack, and for angles of attack from 0° to the post-stall regime at 0.7 Mach number. However, in the specific cases targeted for analysis, there are problems with shocks (location and strength) and boundary layer quantities. ARC2D currently employs the Baldwin-Lomax turbulence model, an easily programmed algebraic formulation. This model has been demonstrated to be accurate enough in many cases, but it is believed that, in some of the cases discussed above, the model is not producing a thick enough boundary layer behind the shock. A correction to this model is being investigated.

## References


1. Beam, R. and Warming, R. F., *An Implicit Finite-Difference Algorithm for Hyperbolic Systems in Conservation Law Form*, J. Comp. Phys. **22** (1976,), 87-110.
2. Steger, J. L., *Implicit Finite Difference Simulation of Flow About Arbitrary Geometries with Application to Airfoils*, AIAA Paper 77-665 (1977).
3. Pulliam, T. H., Jespersen, D. C.,and Childs, R., E., *An Enhanced Version of an Implicit Code for the Euler Equations*, AIAA paper 83-0344 AIAA 21st Aerospace Sciences Meetings, Reno, Nev. (1983).

4. Pulliam, T. H. and Steger, J. L., *Recent Improvements in Efficiency, Accuracy, and Convergence for Implicit Approximate Factorization Algorithms*, AIAA 85-0360 AIAA 23rd Aerospace Sciences Meeting, Reno, Nevada., (1985).
5. Pulliam, T. H., *Efficient Solution Methods for The Navier-Stokes Equations*, Lecture Note for the von Kármán Institute For Fluid Dynamics Lecture Series : Numerical Techniques for Viscous Flow Computation In Turbomachinery Bladings (1985), von Kármán Institute, Rhode-St-Genese, Belgium.
6. Baldwin, B. S. and Lomax, H., *Thin Layer Approximation and Algebraic Model for Separated Turbulent Flows*, AIAA Paper No. 78–257 (1978).
7. Barth, T. J., Pulliam, T. H., and Buning, P. G., *Navier-Stokes Computations for Exotic Airfoils*, AIAA Paper 85-0171 (1985).
8. McDevitt, J. B. and Okuno, A. F., *Static and Dynamic Pressure Measurements on a NACA 0012 Airfoil in the Ames High Reynolds Number Facility*, NASA TP 2485 (1985).
9. Harris, C. D., *Two-Dimensional Aerodynamic Characteristics Of The NACA 0012 Airfoil In the Langley 8-Foot Transonic Pressure Tunnel*, NASA TM - 81927 (1981).
10. Cook, P. , McDonald, M. and Firmin, M., *Aerofoil RAE 2822 - Pressure Distributions, and Boundary layer and Wake Measurements*, AGARD- AR- 138 (1979).

Figure 1 - 369 x 65 C-grid for NACA 0012 airfoil

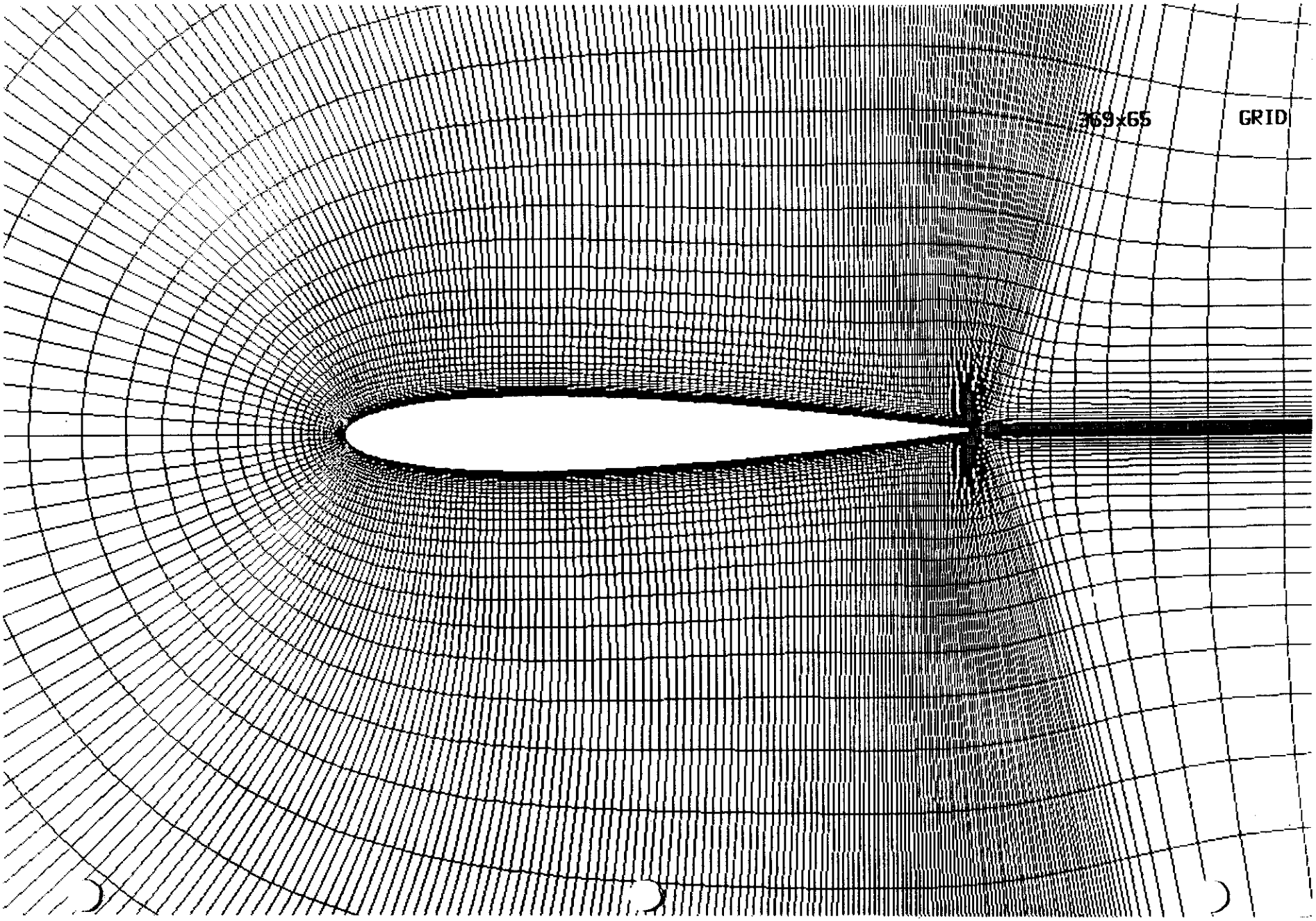

Figure 2 – Coefficient of pressure vs. x/c for case A1

NACA 0012

M = 0.7, alpha = 1.49, exp. alpha = 1.86

Cl = 0.254, Cd = .0083

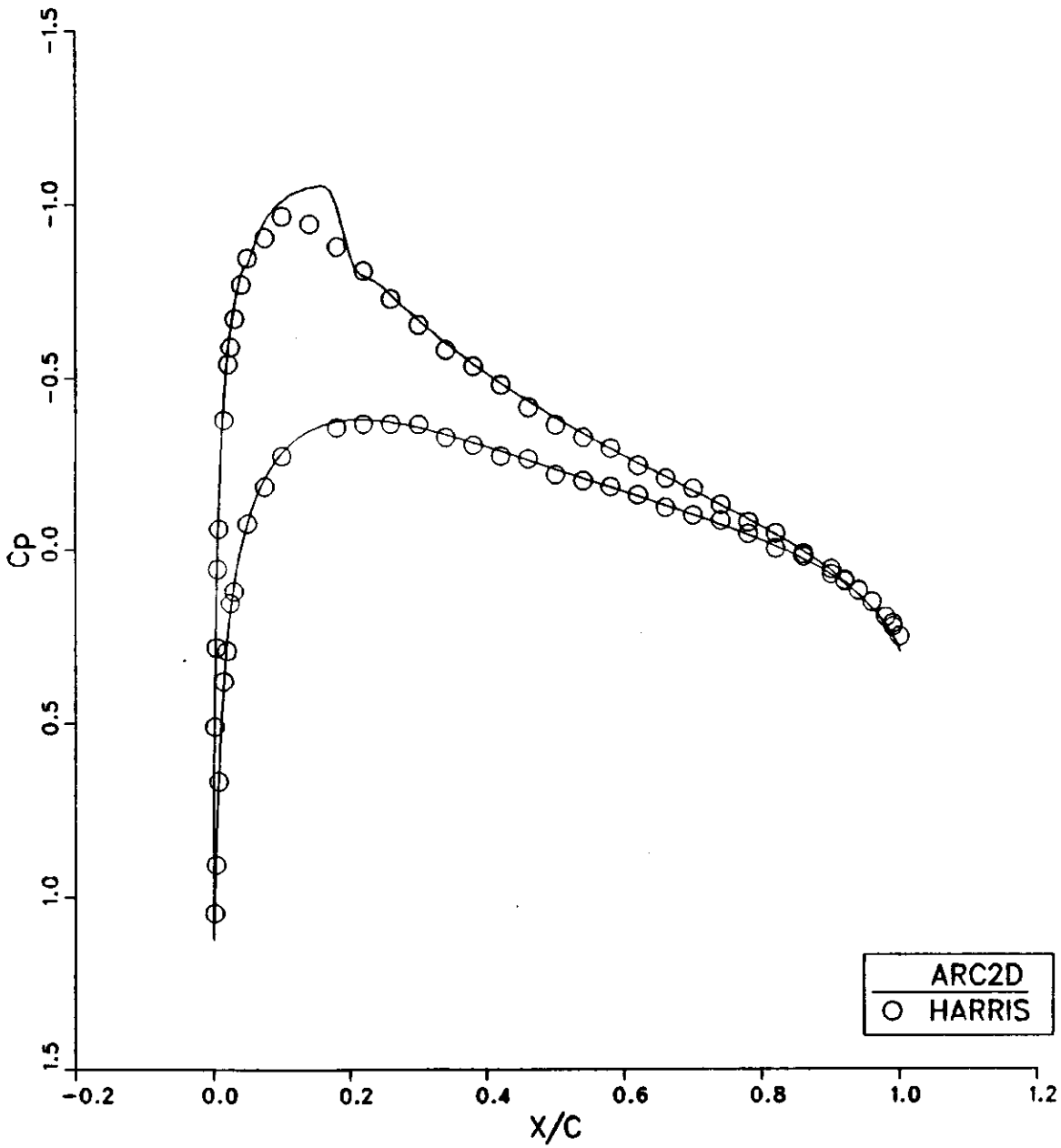

Figure 3 – Mach contours for case A1

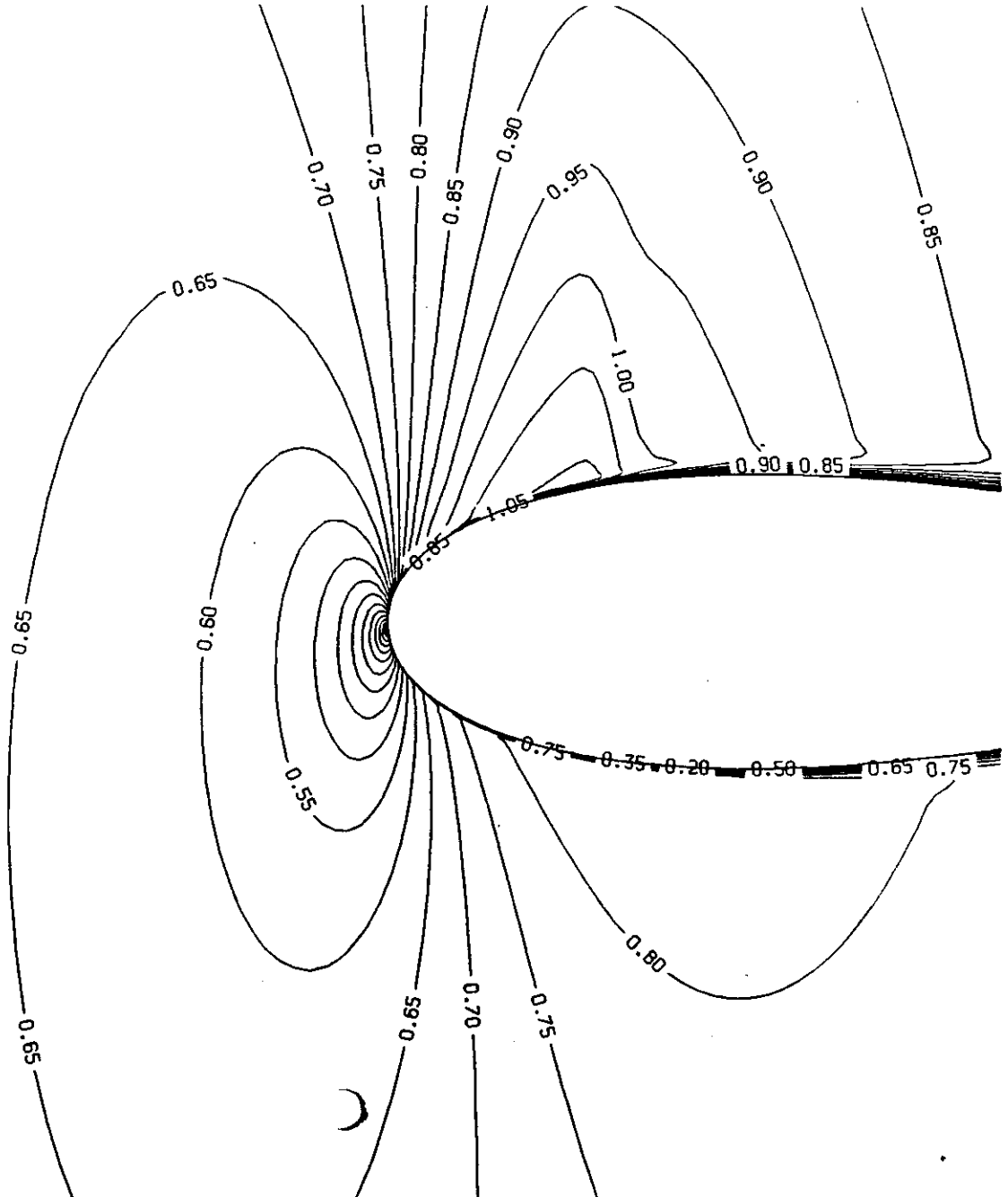

Figure 4 – Coefficient of pressure vs. x/c for case A2
NACA 0012
M = 0.55, alpha = 8.34, exp. alpha = 9.86
Cl = 0.988, Cd = 0.0362

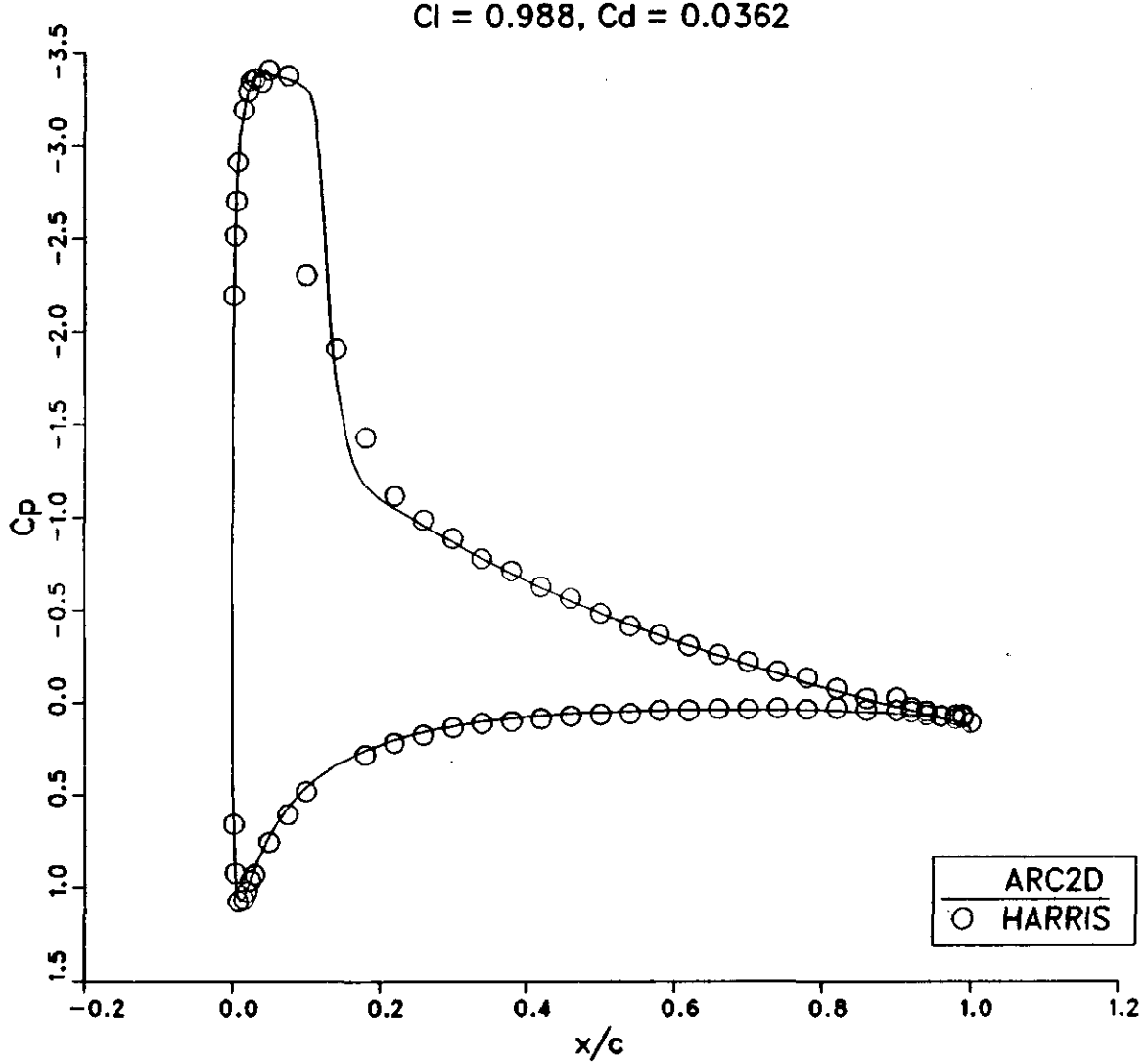

Figure 5 – Coefficient of pressure vs. x/c for case A3

NACA 0012

M = 0.799, alpha = 2.26, exp. alpha = 2.86

Cl = 0..472, Cd = .0445

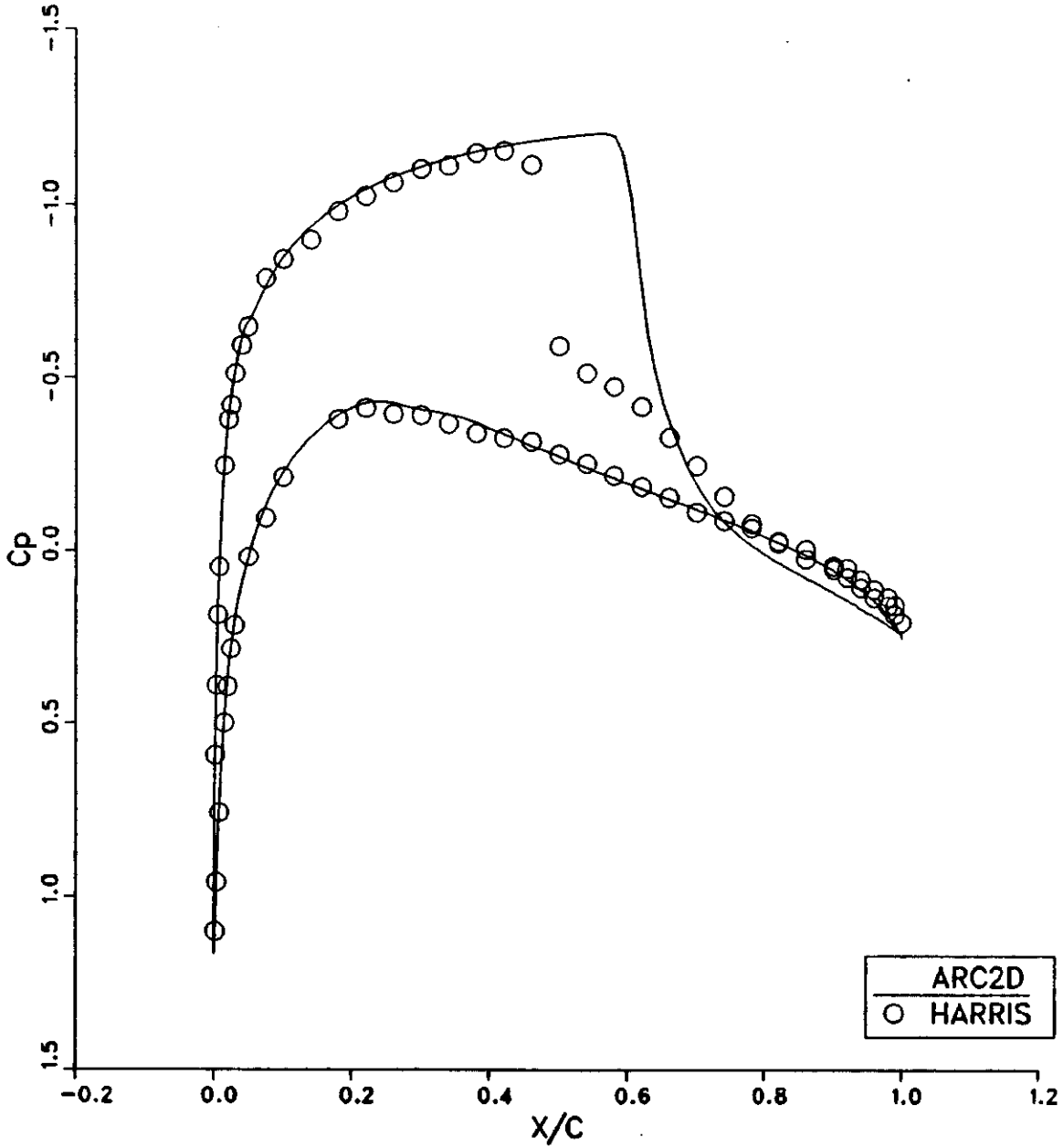

Figure 6 – Cp with variations in dissipation

NACA 0012

M = 0.799, ALPHA = 2.26

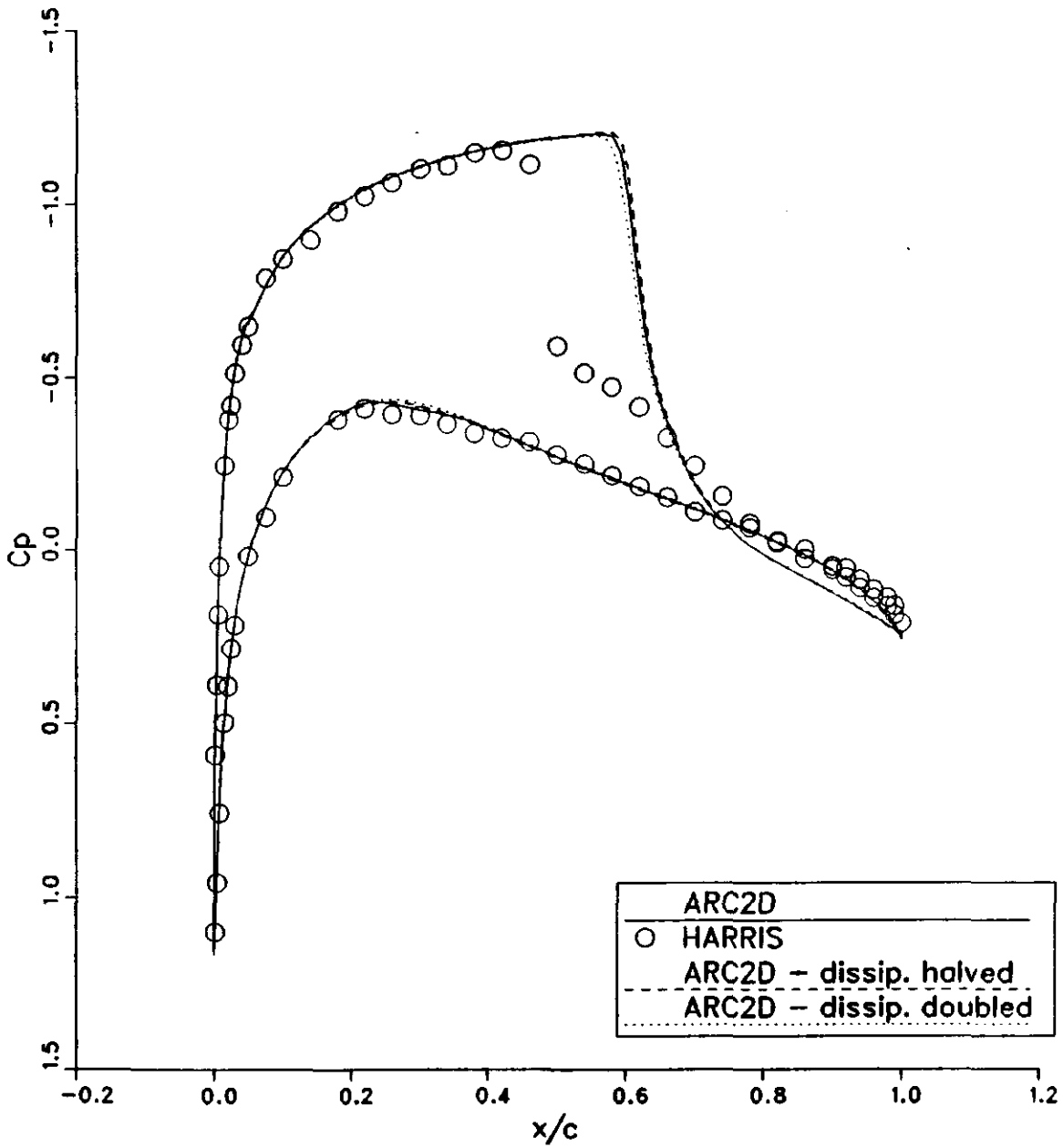

Figure 7 – Lift coefficient vs. angle of attack for case A4
NACA 0012
M = 0.7

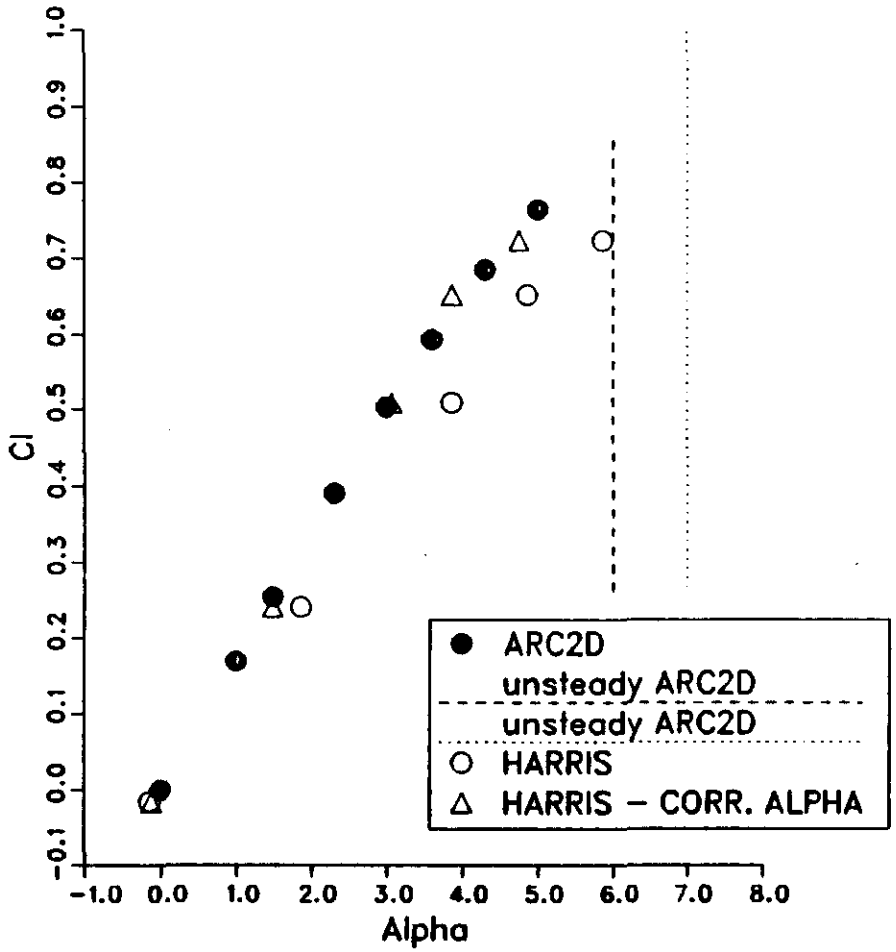

Figure 8 - Lift coefficient vs. iteration

NACA 0012

M = 0.7, alpha = 6.0

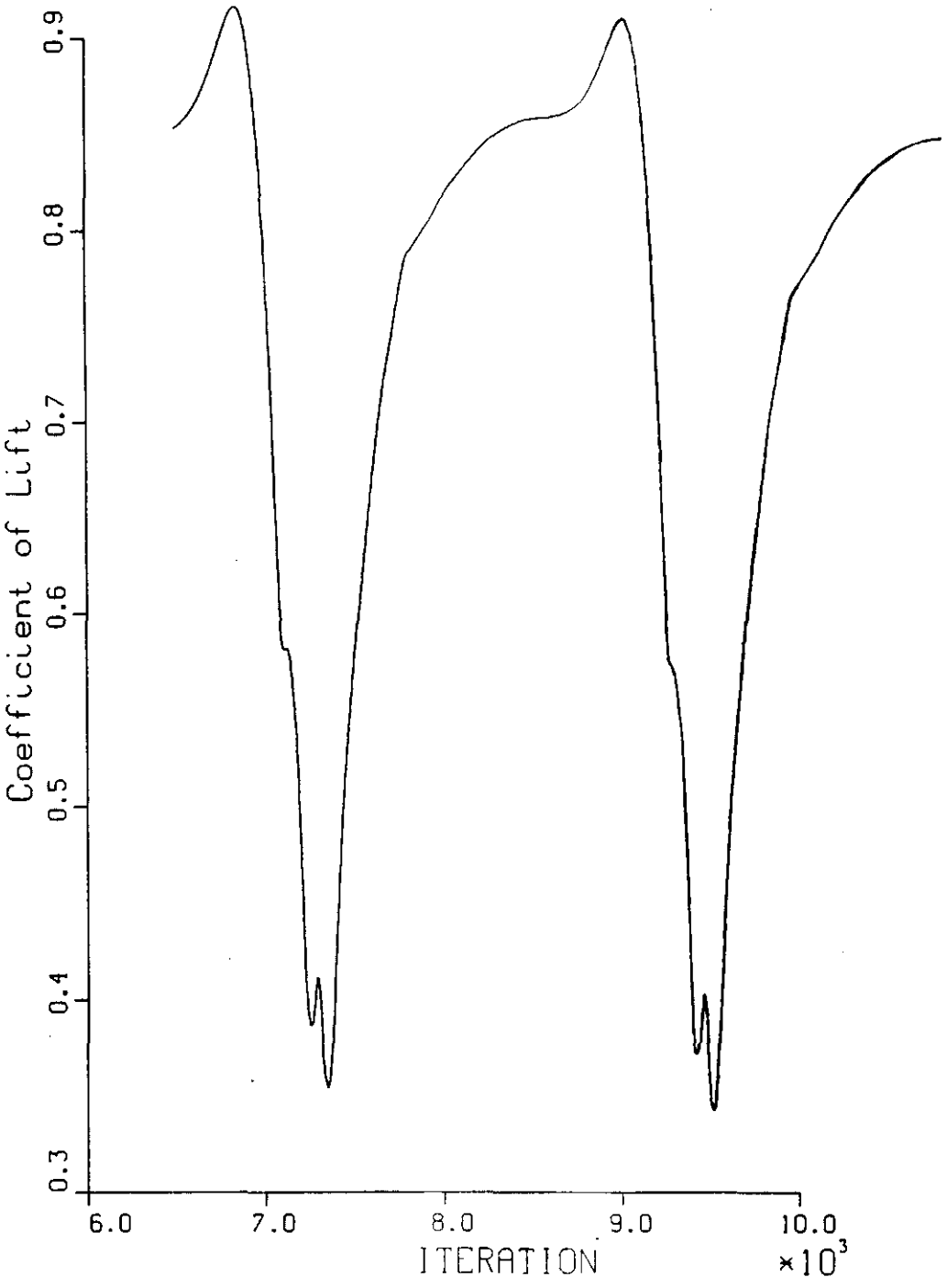

Figure 9 – Lift coefficient vs. drag coefficient, case A5
NACA 0012
M = 0.7

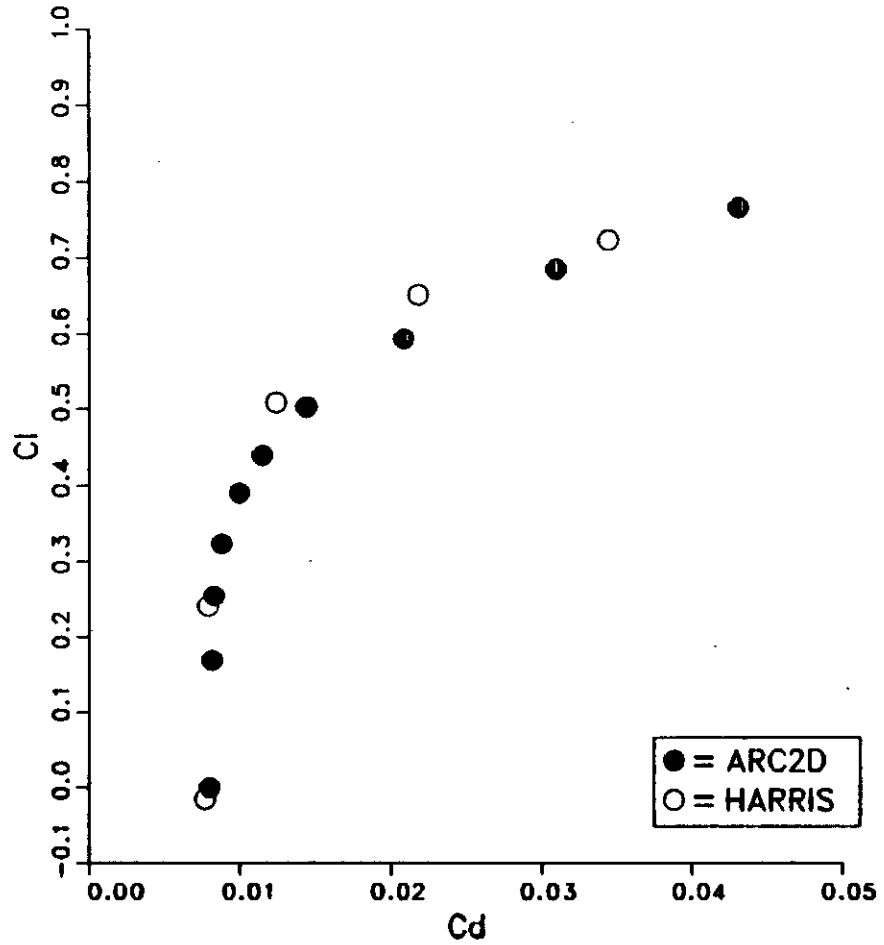

Figure 10 – Drag coefficient vs. Mach number for case A6

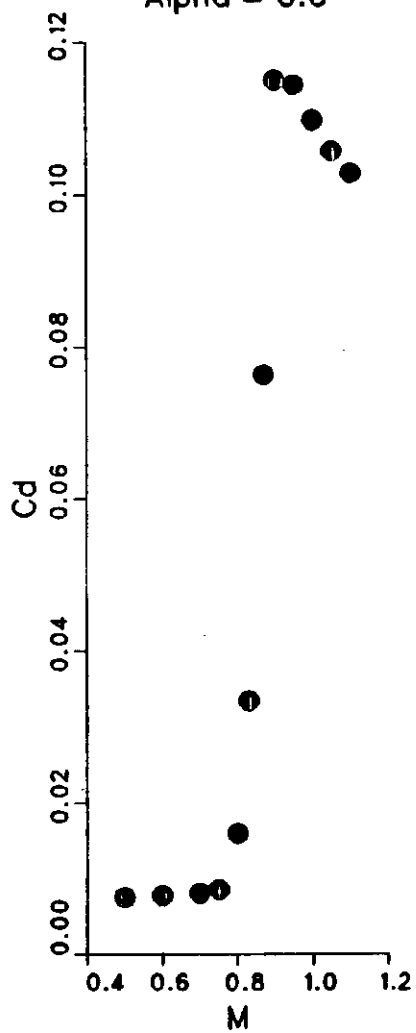

Figure 11 – CI vs. del for grid refinement study, case A7
NACA 0012
M = 0.7, alpha = 1.49

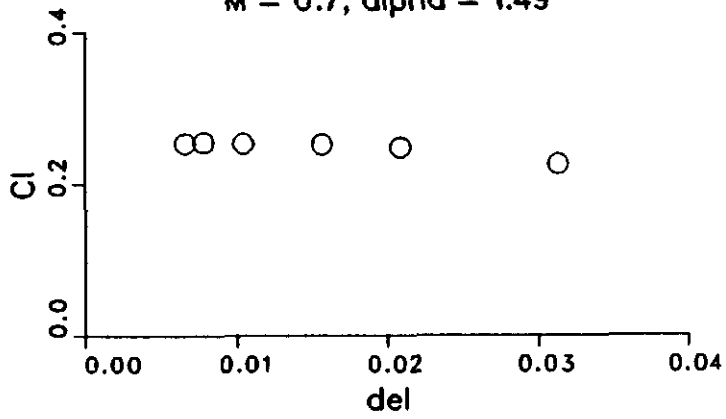

Figure 12 – Cd vs. del for grid refinement study, case A8
NACA 0012
M = 0.7, alpha = 1.49

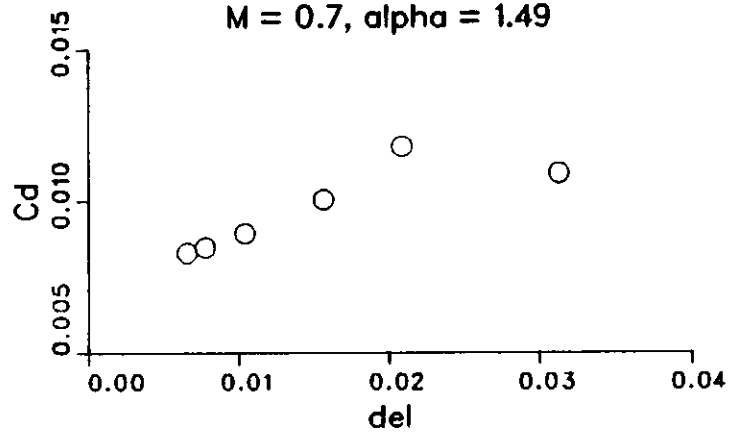

Figure 13 – Cl vs. R for outer boundary study, case A9
NACA 0012
M = 0.7, alpha = 1.49

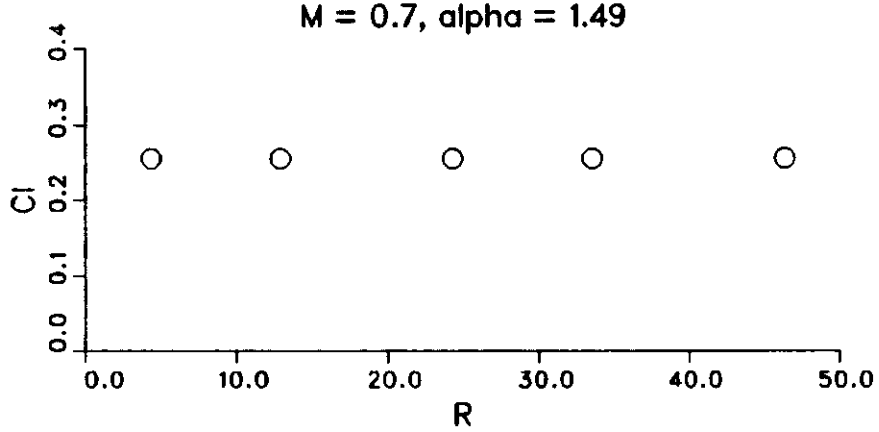

Figure 14 – Cd vs. R for outer boundary study, case A10
NACA 0012
M = 0.7, alpha = 1.49

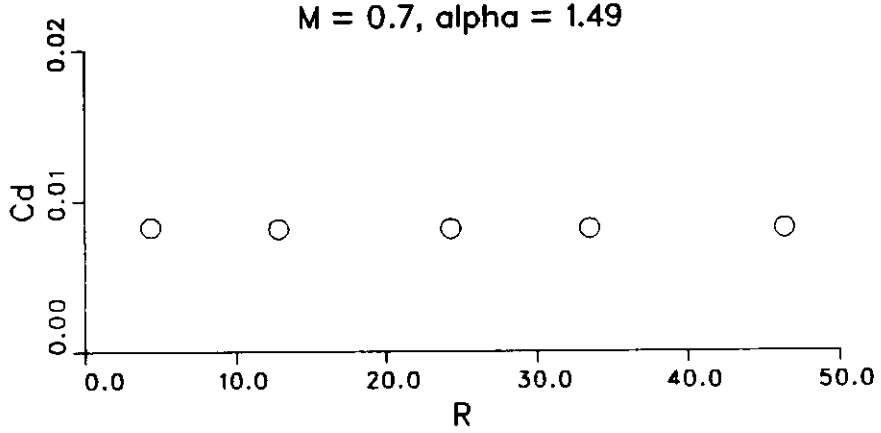

Figure 15 – 369 x 65 C–grid for RAE 2822 airfoil

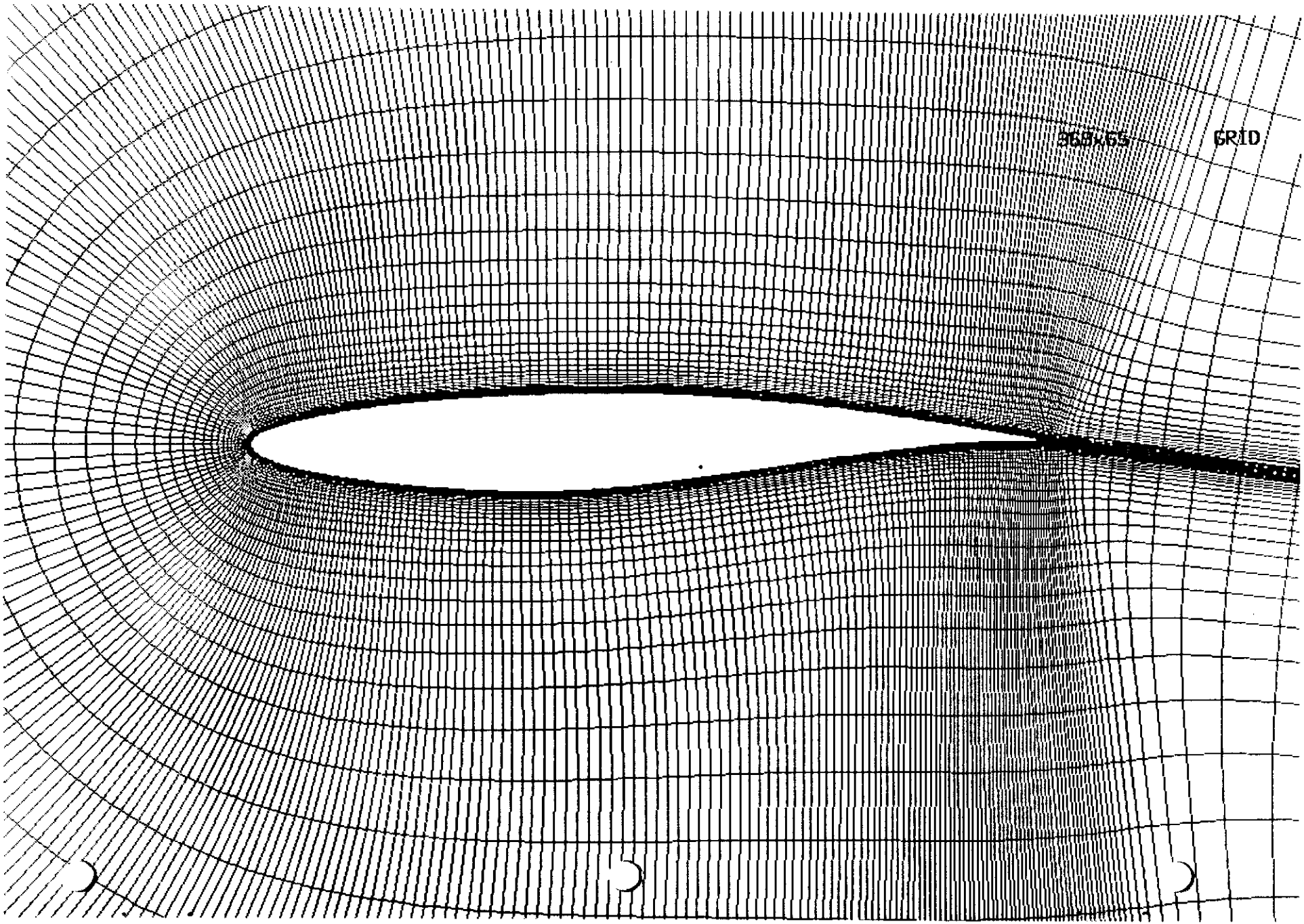

Figure 16 – Coefficient of pressure vs. x/c for case B1

RAE 2822

M = 0.725, alpha = 2.30, exp. alpha = 2.92

Cl = 0.747, Cd = 0.0123

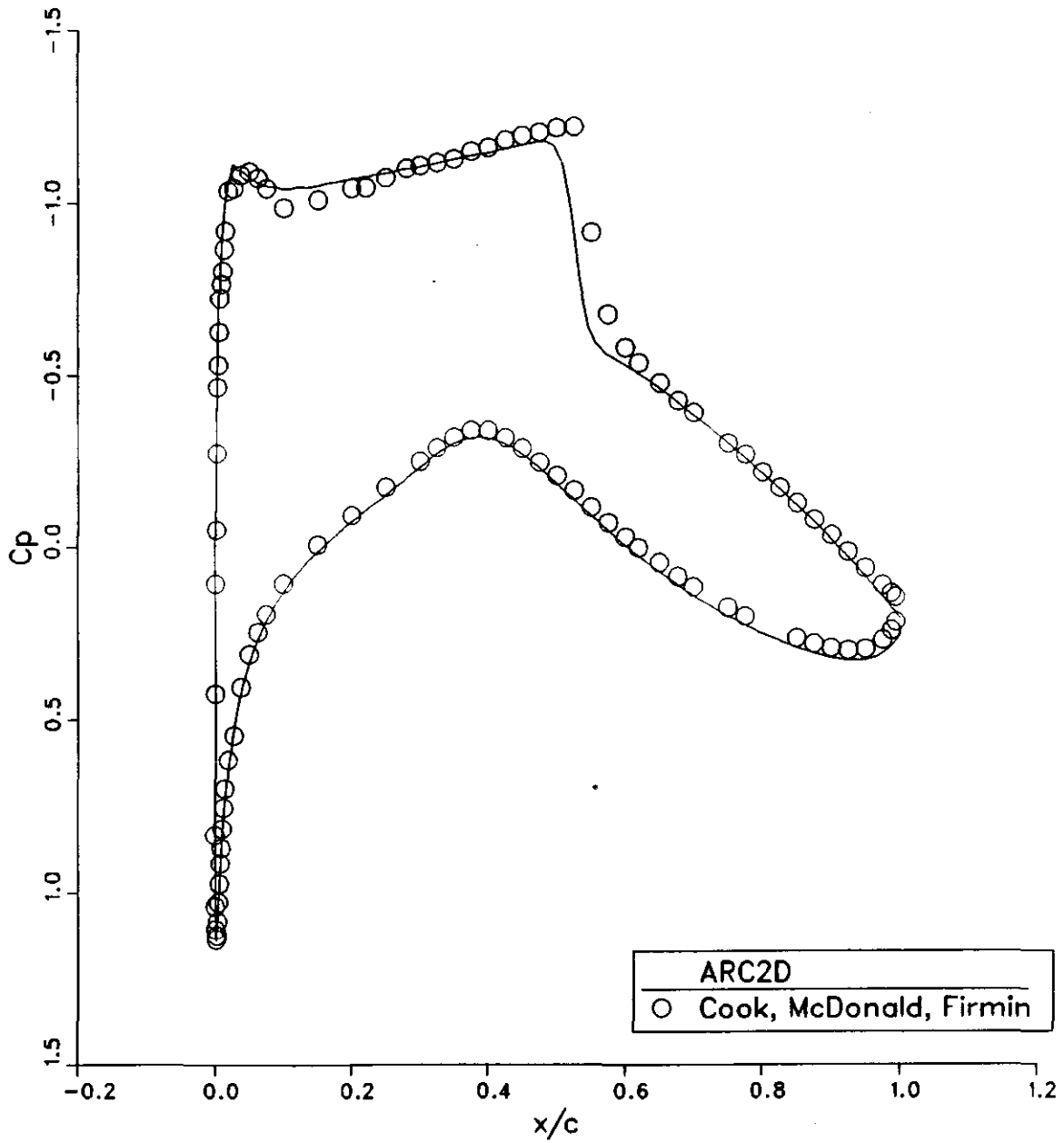

Figure 17 – Momentum thickness vs. x/c for case B2
RAE2822
M = .725, alpha = 2.3

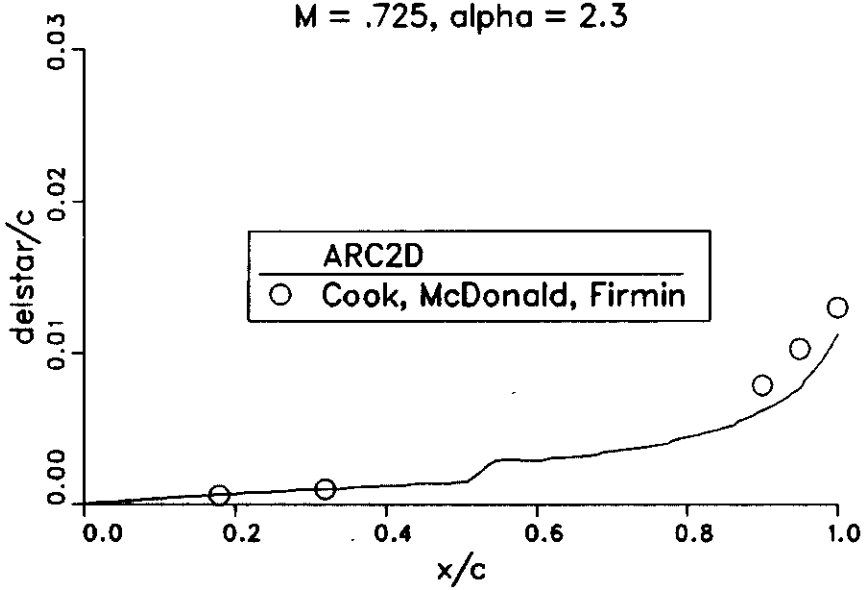

Figure 18 – Skin friction coefficient vs. x/c for case B3



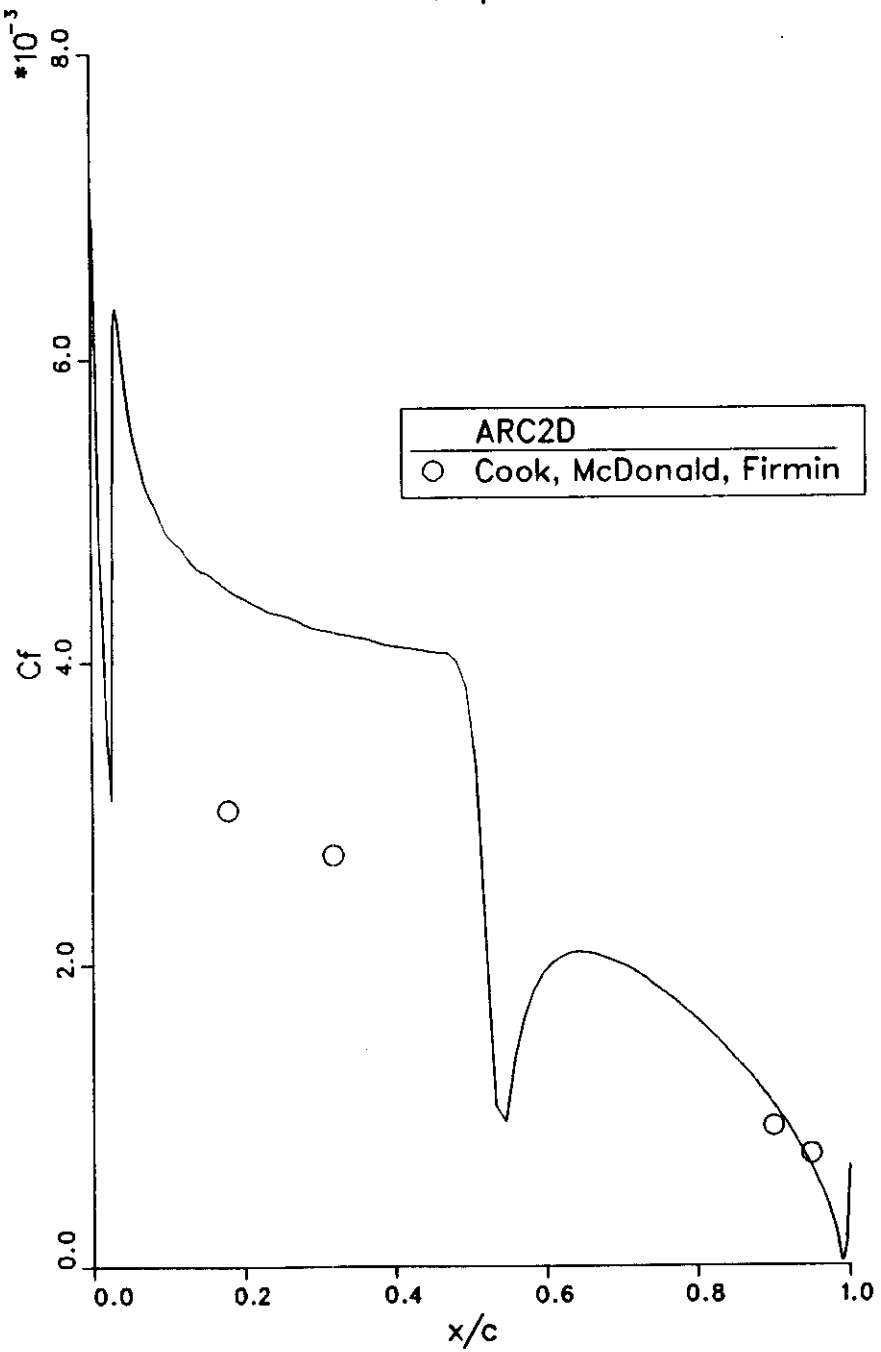

Figure 19a – Boundary layer profile at x/c = 0.319, case B4
RAE 2822
M = 0.725, alpha = 2.30

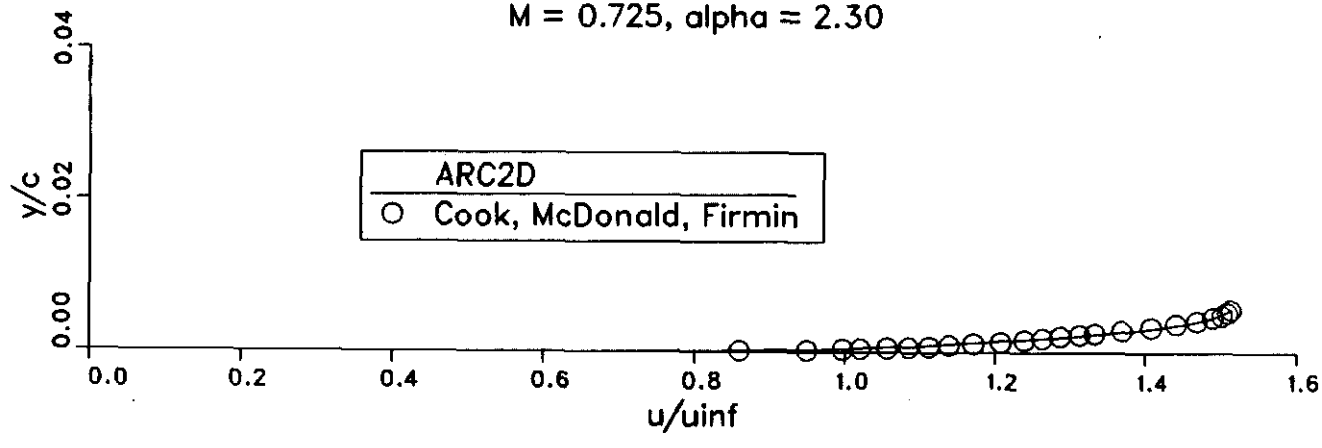

Figure 19b – Boundary layer profile at x/c = 0.319, case B4
RAE 2822
M = 0.725, alpha = 2.30

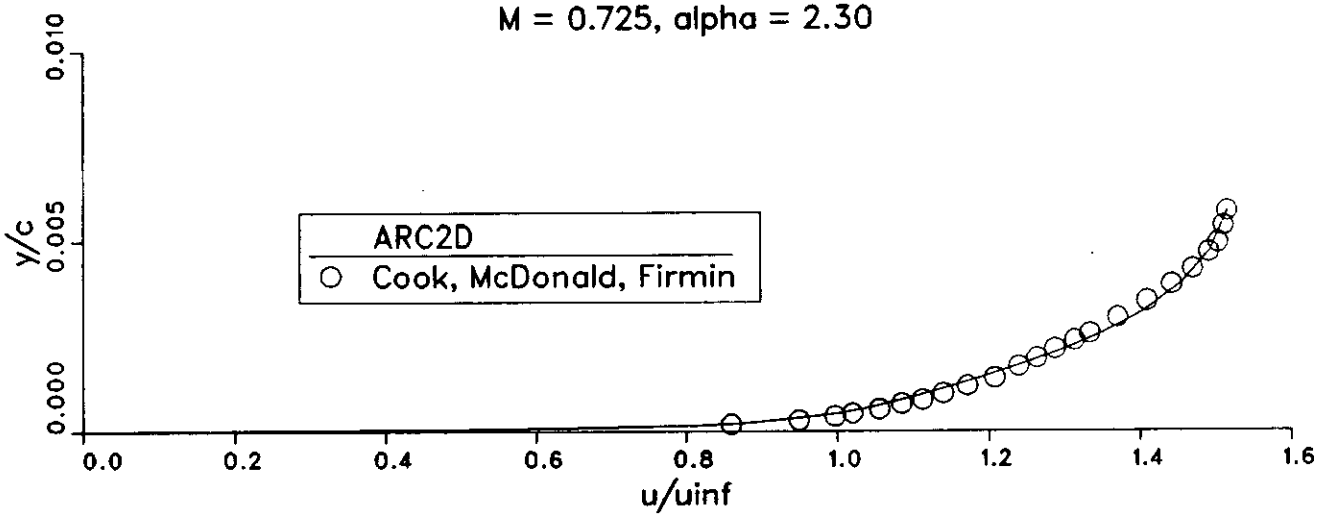

Figure 20 – Boundary layer profile at x/c = 0.95, case B5
RAE 2822
M = 0.725, alpha = 2.30

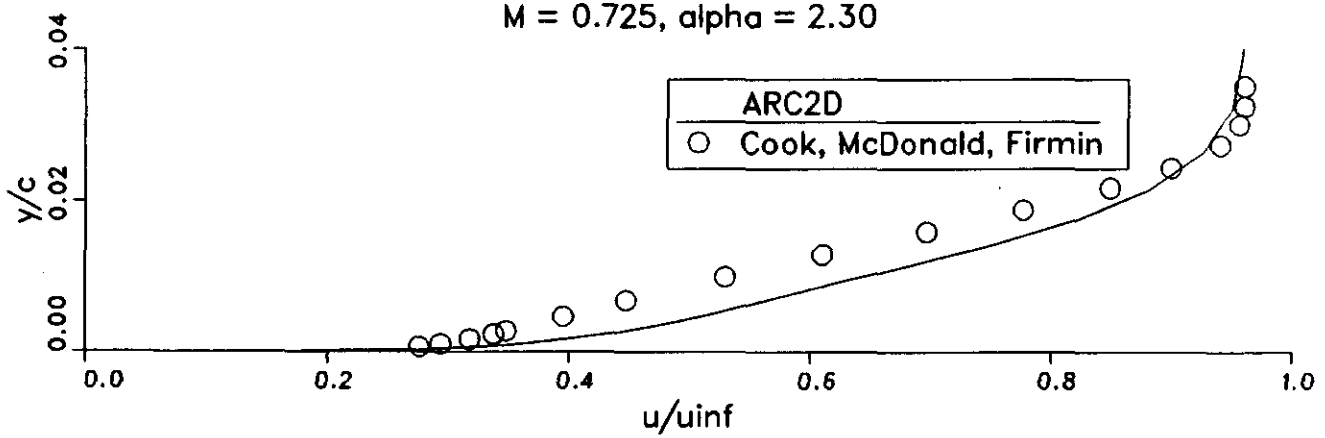

Figure 21 – Coefficient of pressure vs. x/c for case B6

RAE 2822

M = 0.75, alpha = 2.72, exp. alpha = 3.19

Cl = 0.838, Cd = 0.0289

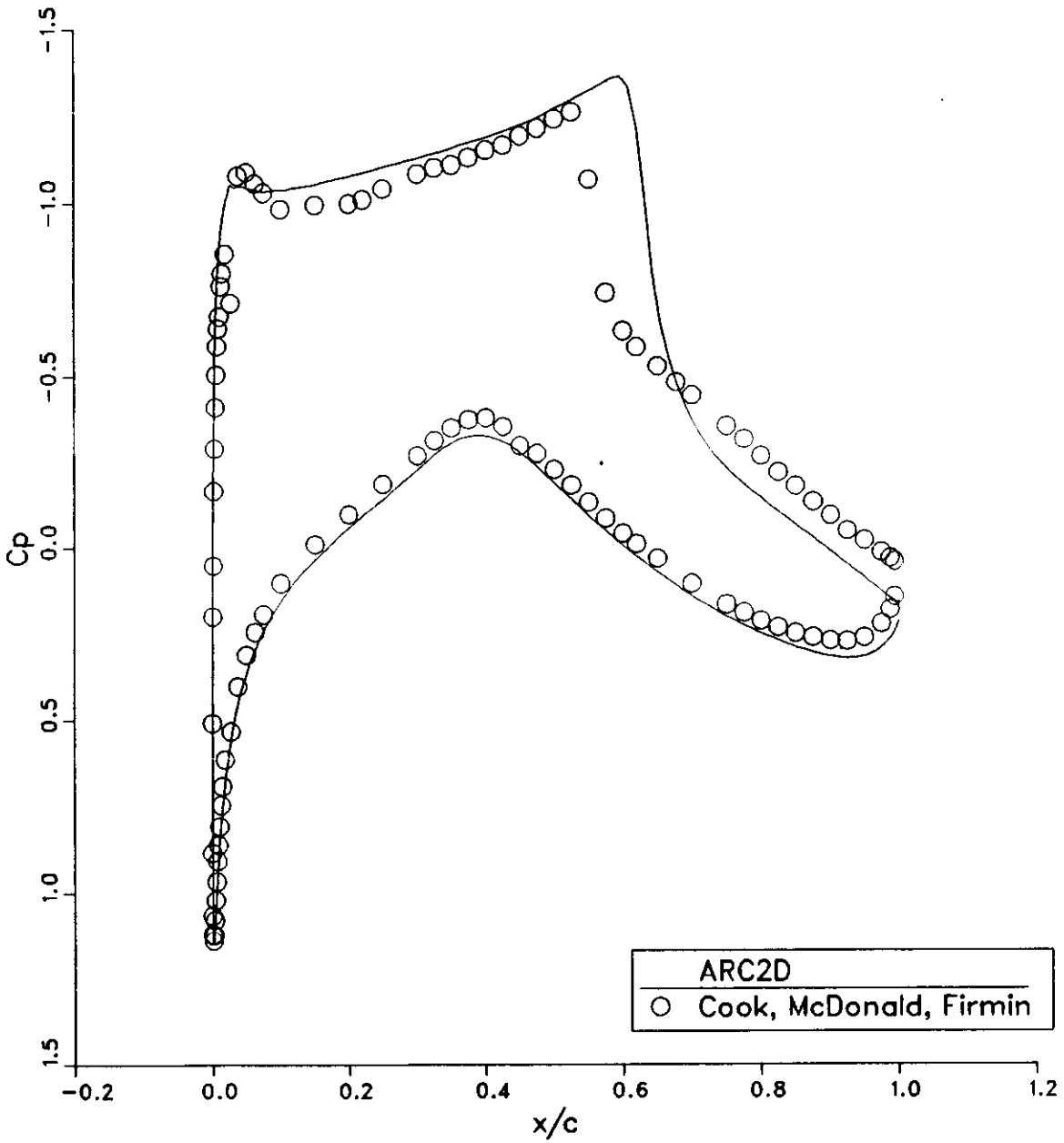

Figure 22 – Momentum thickness vs. x/c for case B7
RAE 2822
M = 0.75, alpha = 2.72

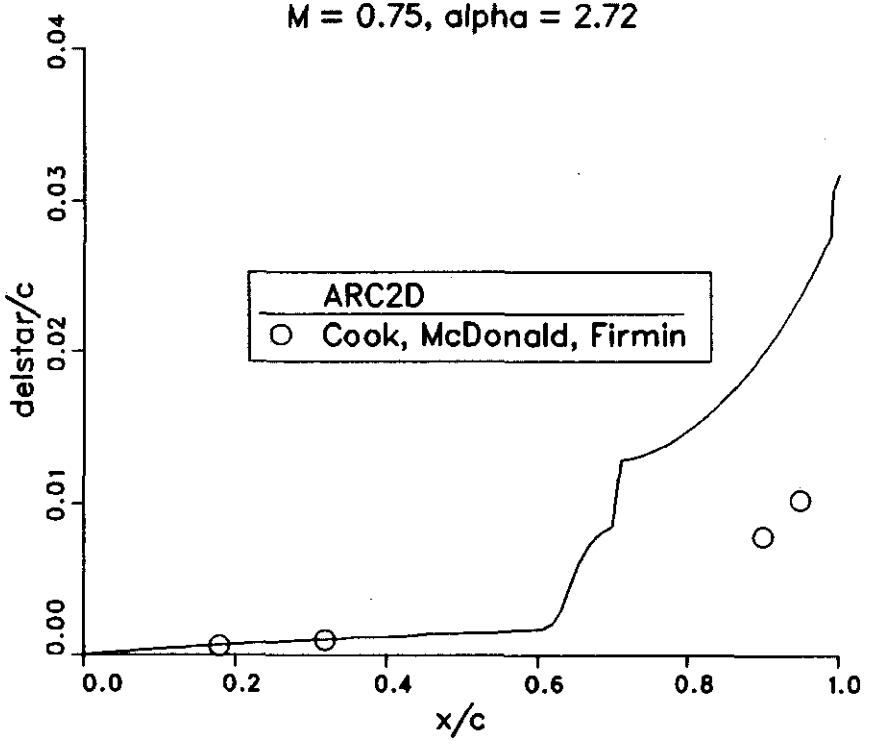

Figure 23 – Skin friction coefficient vs. x/c for case B8

RAE 2822

M = 0.75, alpha = 2.72

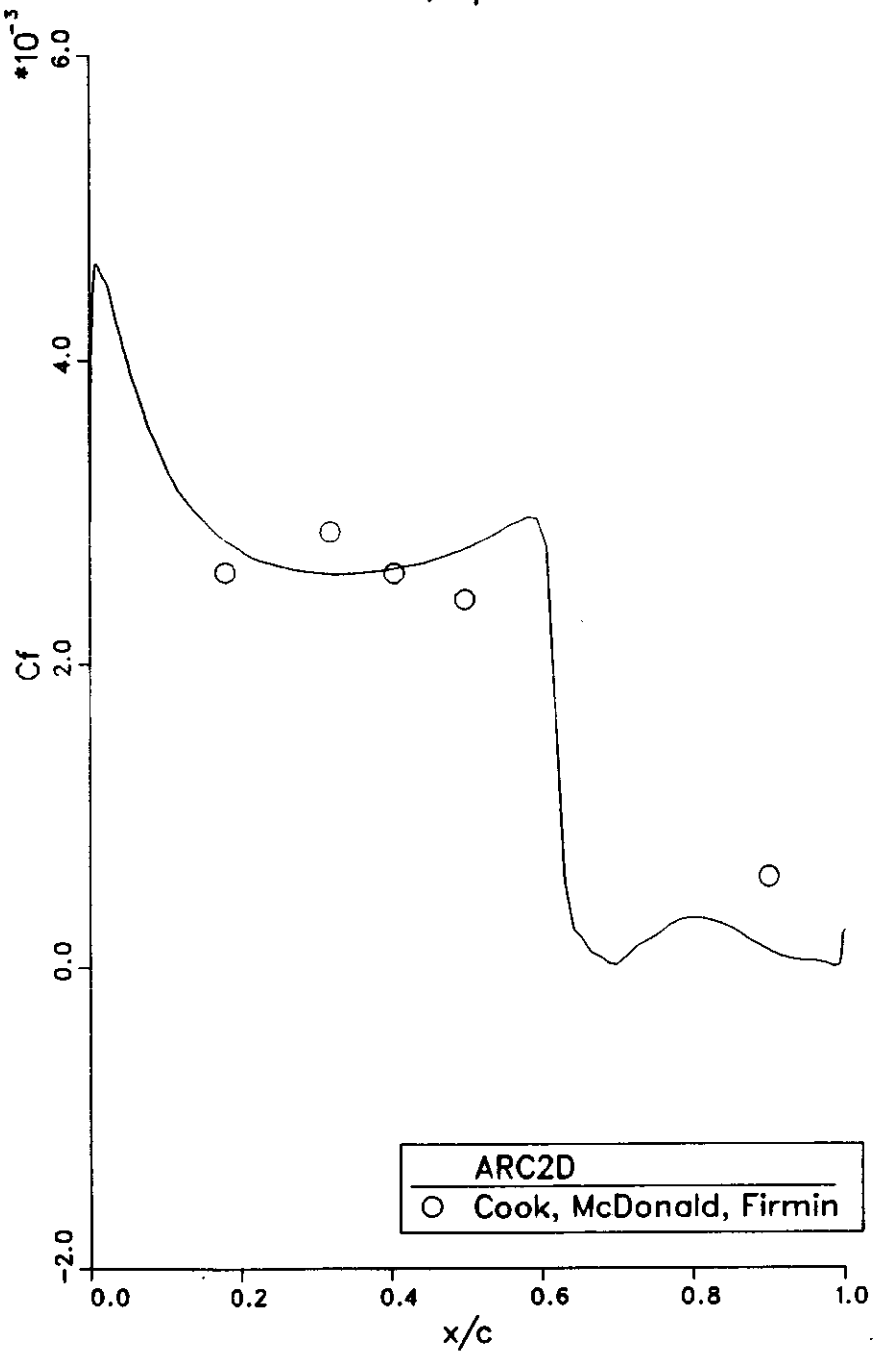

Figure 24 – Boundary layer profile at x/c = 0.75, case B9
RAE 2822
M = 0.75, alpha = 2.72

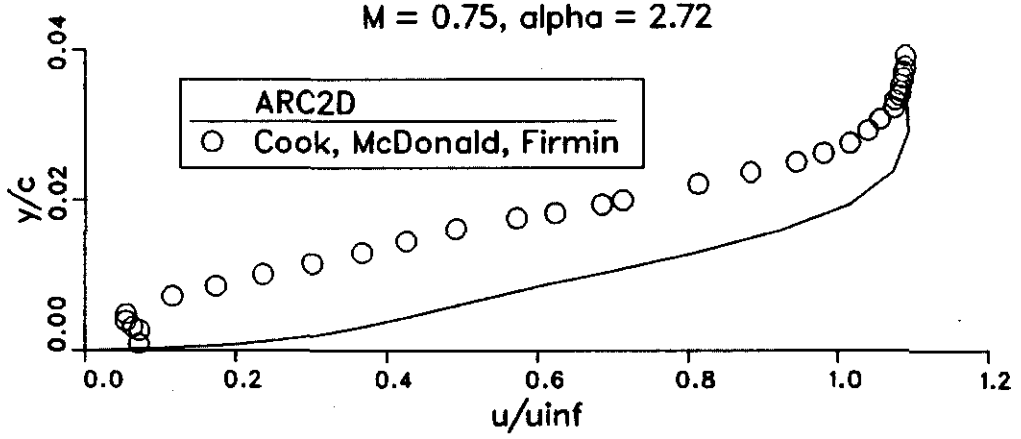

Figure 25 – Boundary layer profile at x/c = 0.9, case B10
RAE 2822
M = 0.75, alpha = 2.72

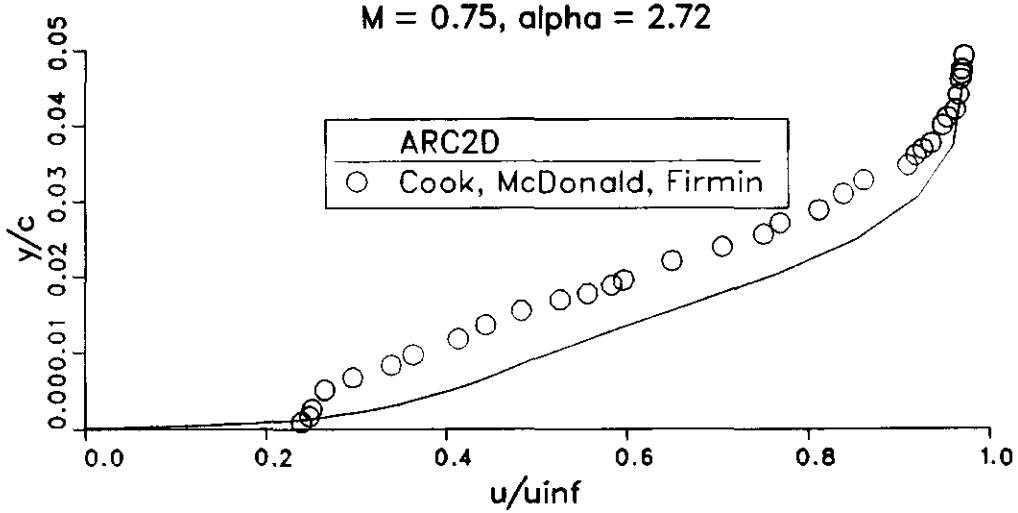

Figure 26 – Sonic line for case B11
RAE 2822
M = 0.75, alpha = 2.72

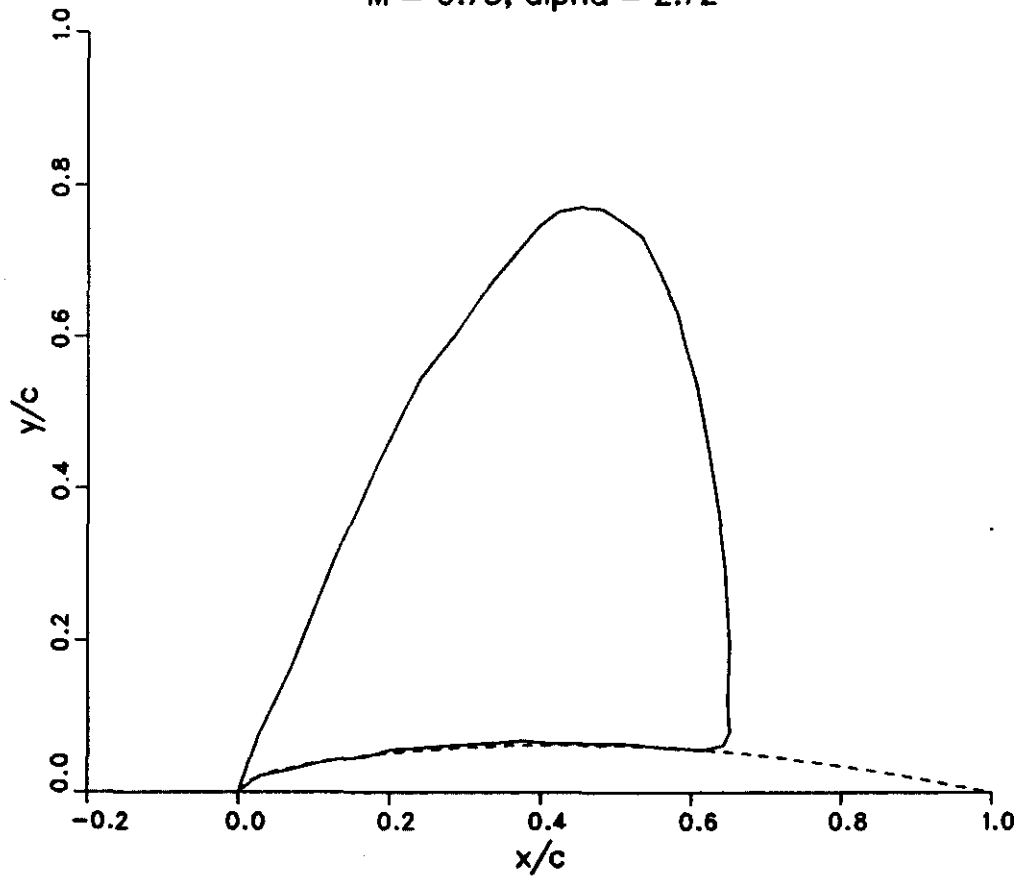

Figure 27 – 369 x 65 C–grid for Jones airfoil

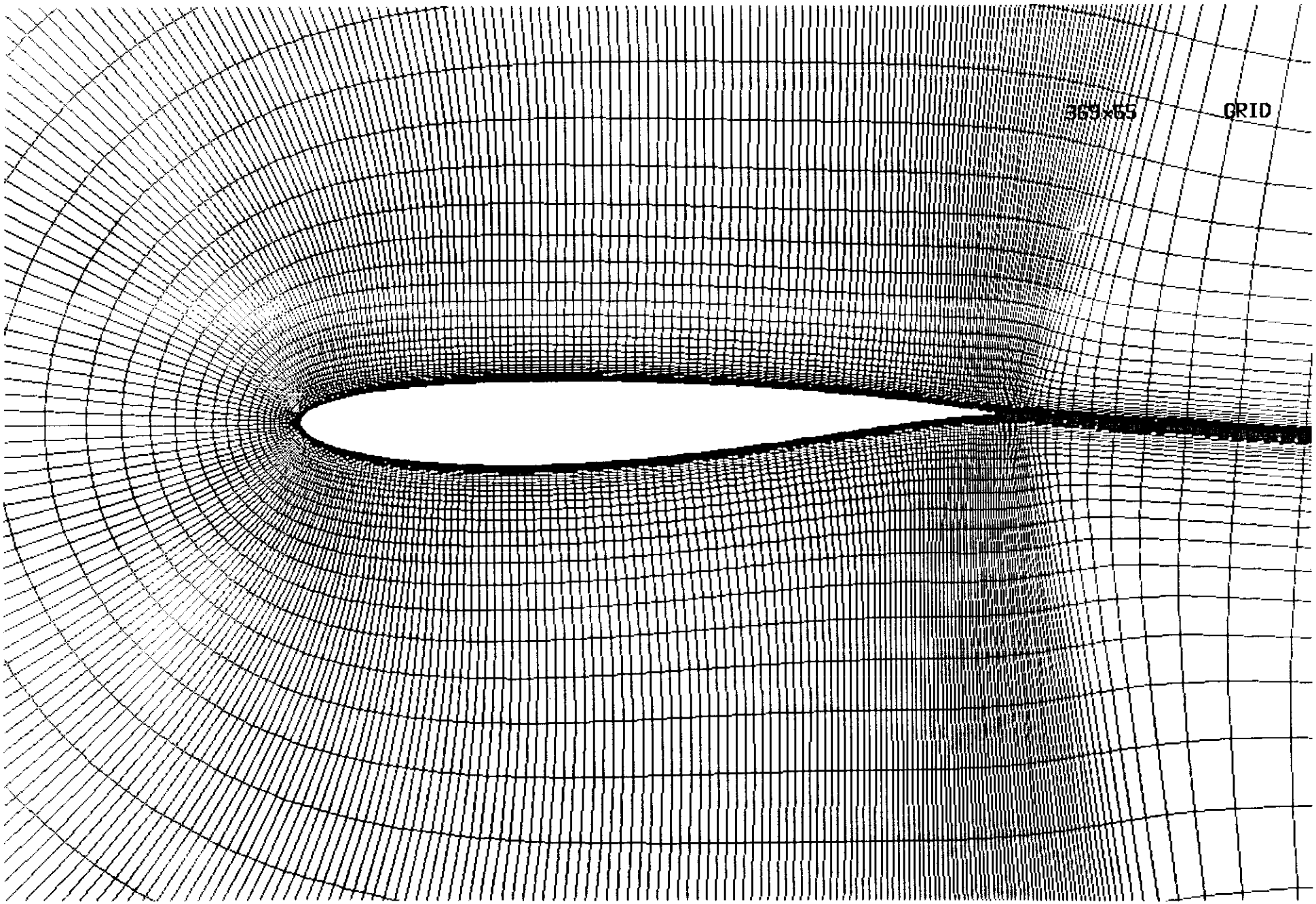

Figure 28 – Lift coefficient vs. angle of attack, case C1

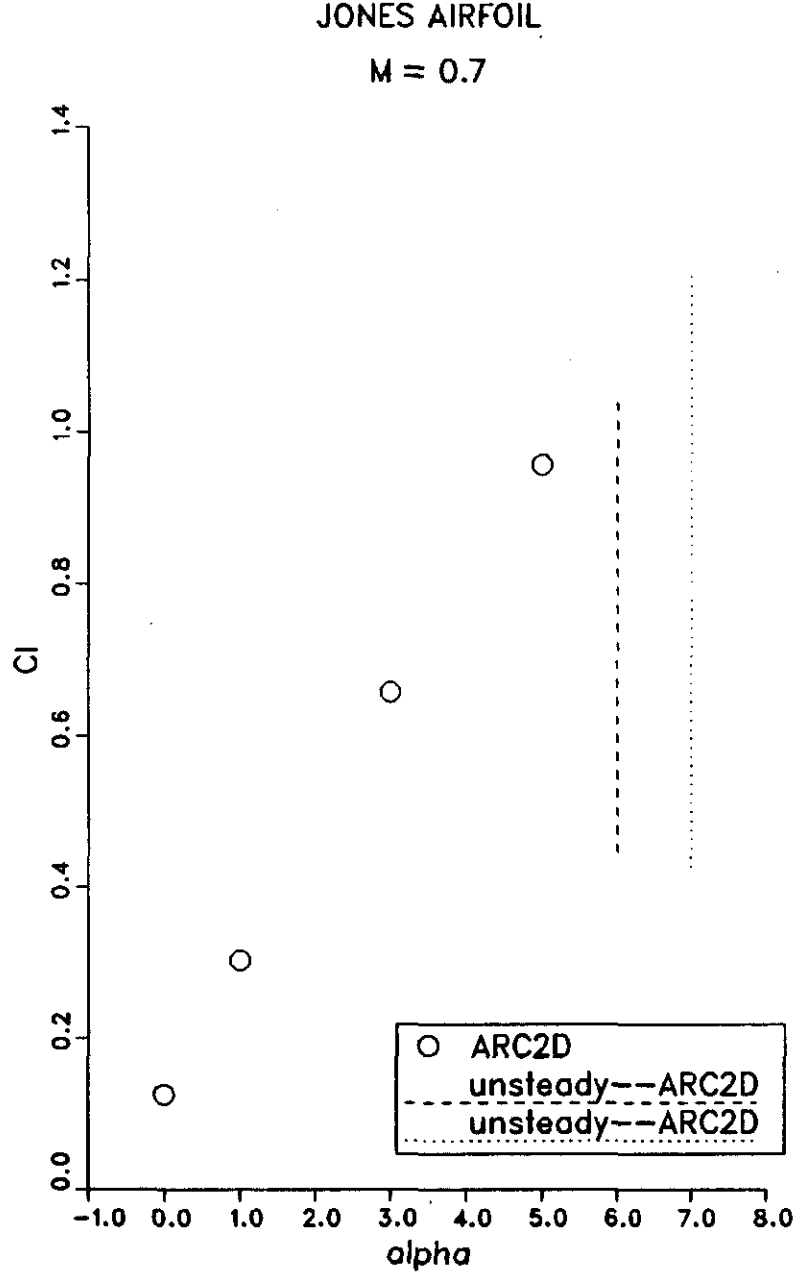

Figure 29 - Lift coefficient vs. iteration

Jones airfoil

M = 0.7, alpha = 6.0

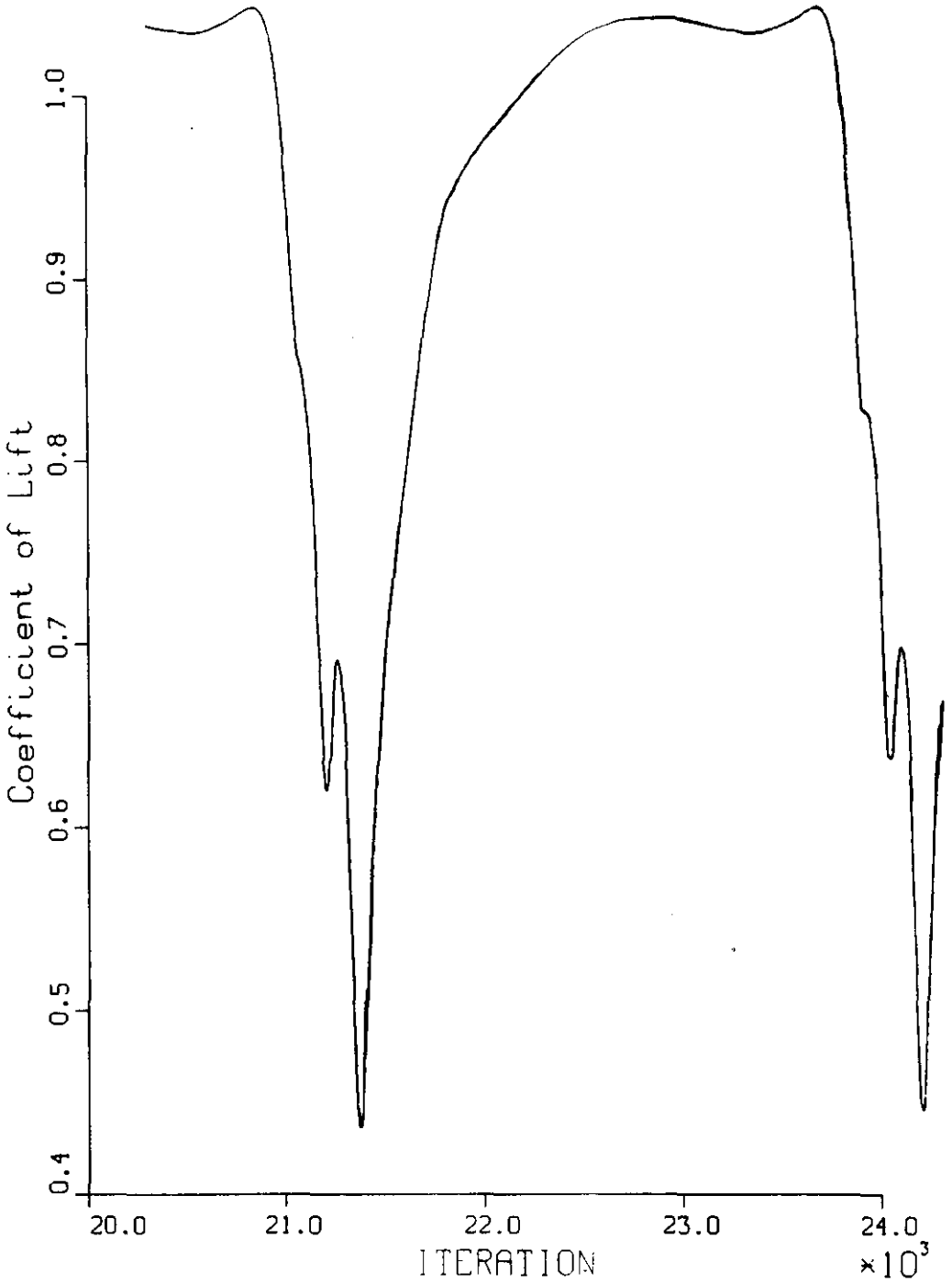

Figure 30 – Lift coefficient vs. drag coefficient, case C2
JONES AIRFOIL
M = 0.7

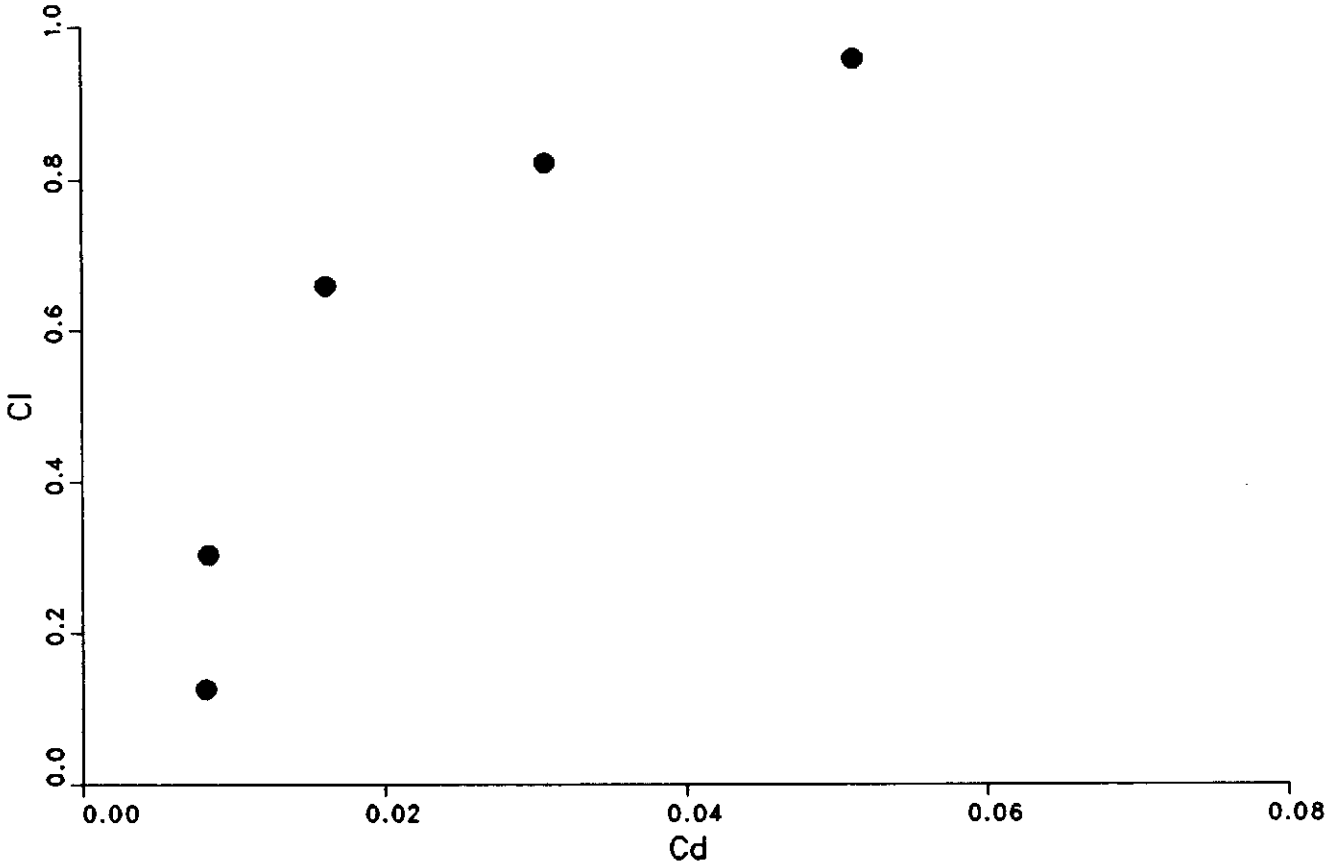

Figure 31 – Drag coefficient vs. Mach number for case C3

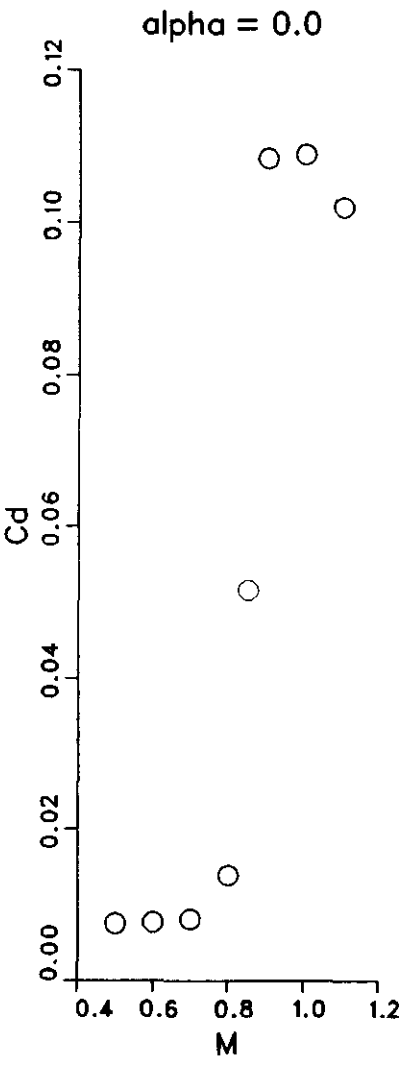

Figure 32 – Coefficient of pressure vs. x/c for case C4

JONES AIRFOIL

M = 0.75, alpha = 2.0

Cl = 0.558, Cd = 0.0178

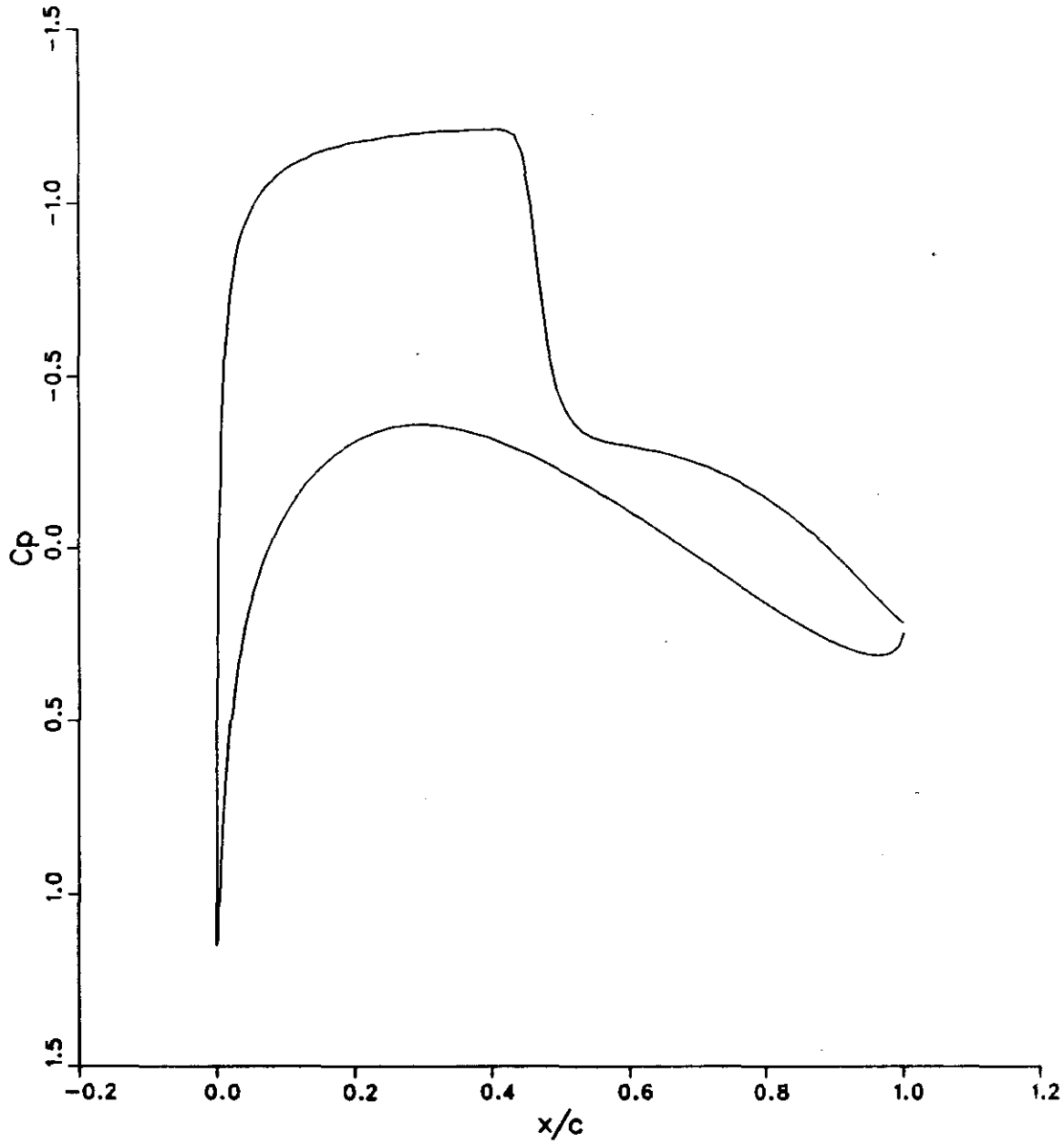

Figure 33 – Momentum thickness vs. x/c for case C5
JONES AIRFOIL
M = 0.75, alpha = 2.0

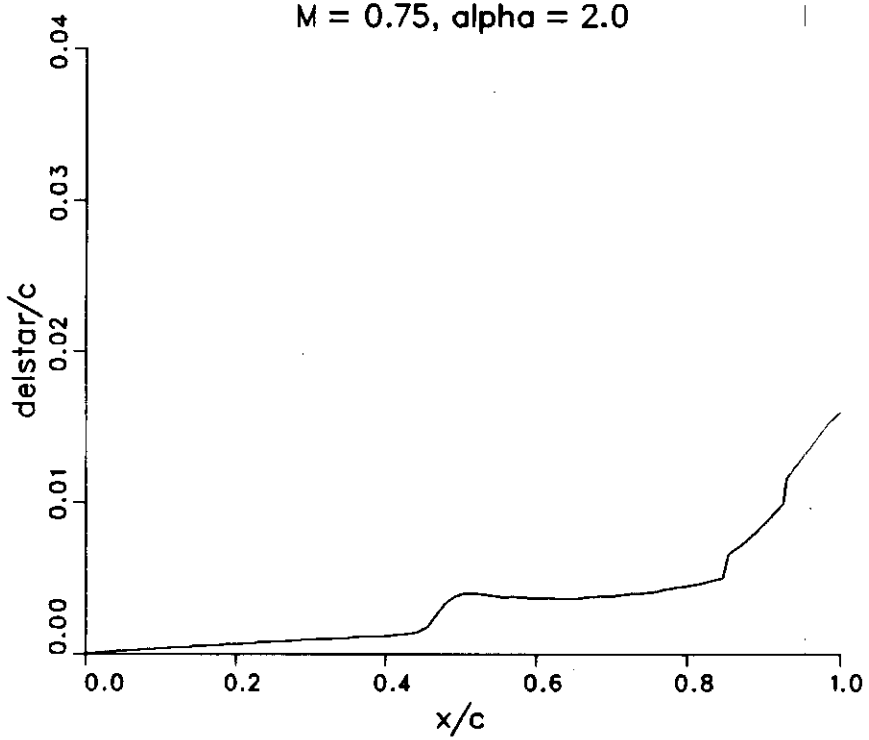

Figure 34 – Skin friction coefficient vs. x/c for case C6

JONES AIRFOIL

M = 0.75, alpha = 2.0

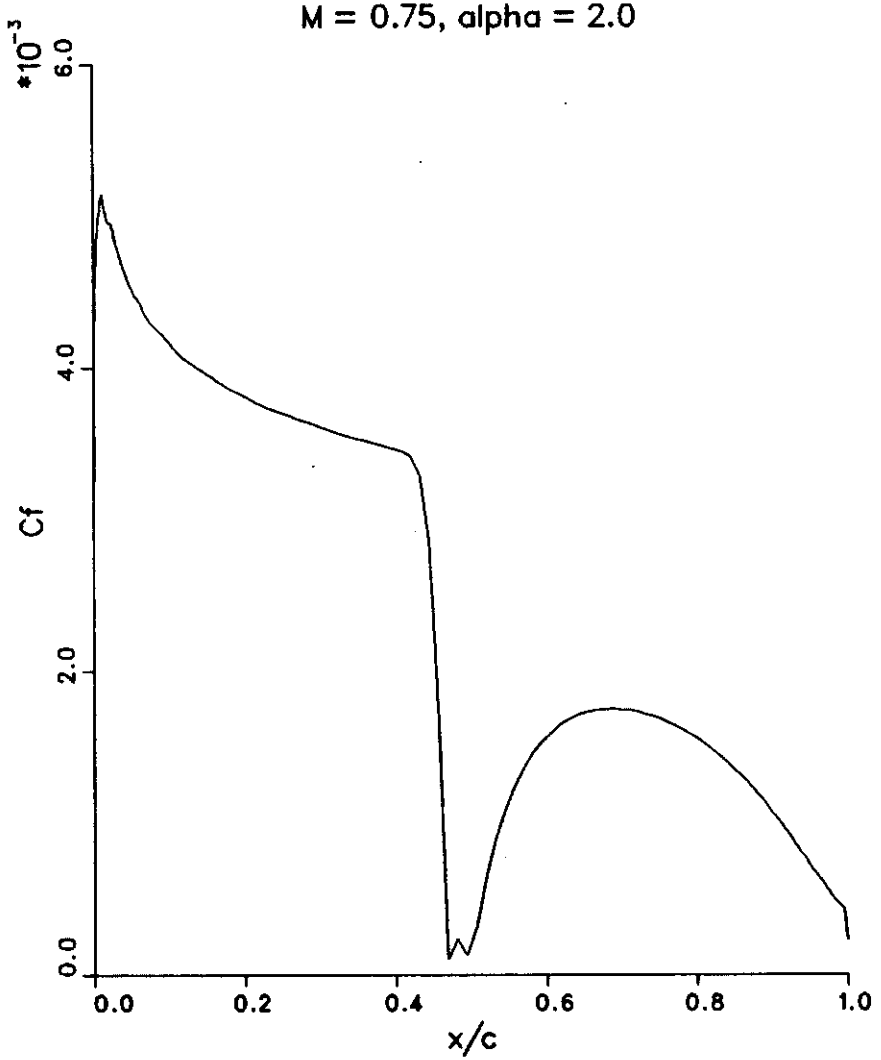

Figure 35a – Boundary layer profile at x/c = 0.6, case C7
JONES AIRFOIL
M = 0.75, alpha = 2.0

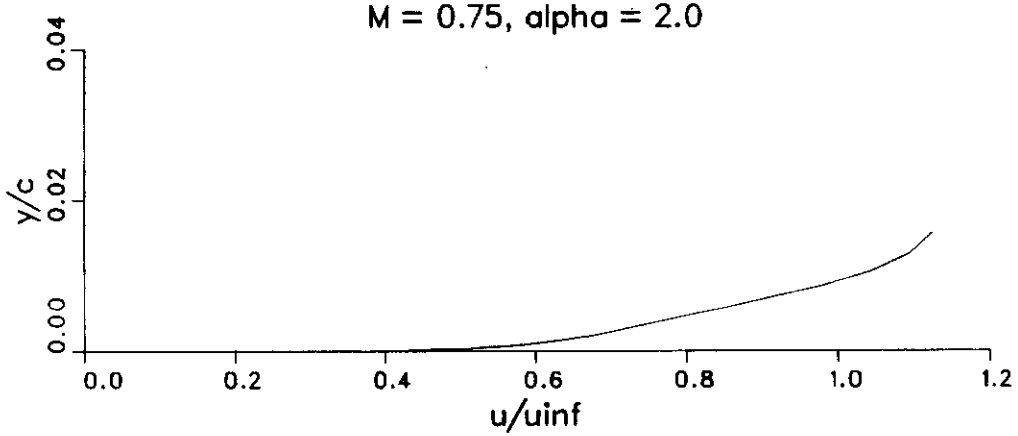

Figure 35b – Boundary layer profile at x/c = 0.6, case C7
JONES AIRFOIL
M = 0.75, alpha = 2.0

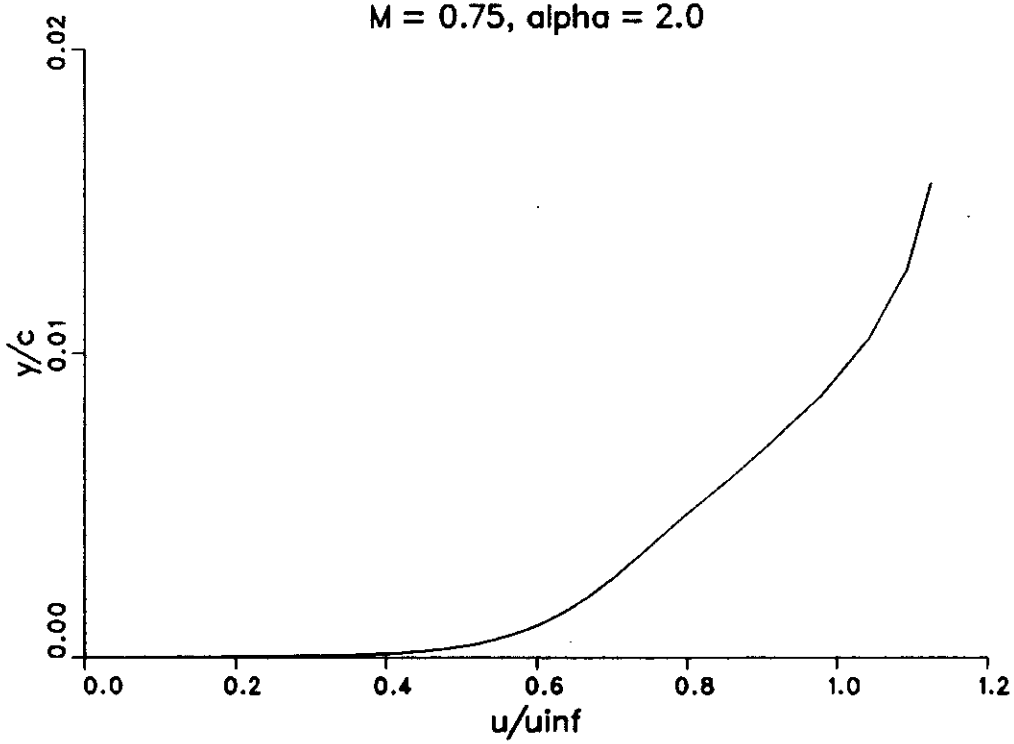

Figure 36 – Boundary layer profile at x/c = 0.9, case C8

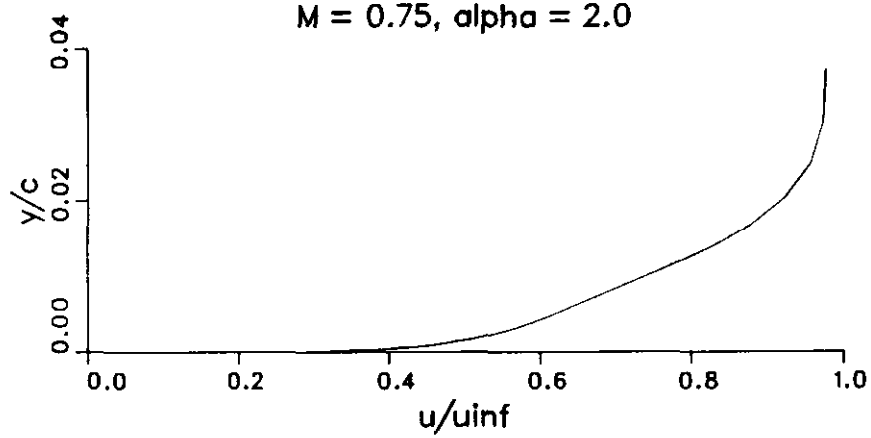

Figure 37 – Coefficient of pressure vs. x/c for case C9

JONES AIRFOIL

M = 0.85, alpha = 2.0

Cl = 0.285, Cd = .0599

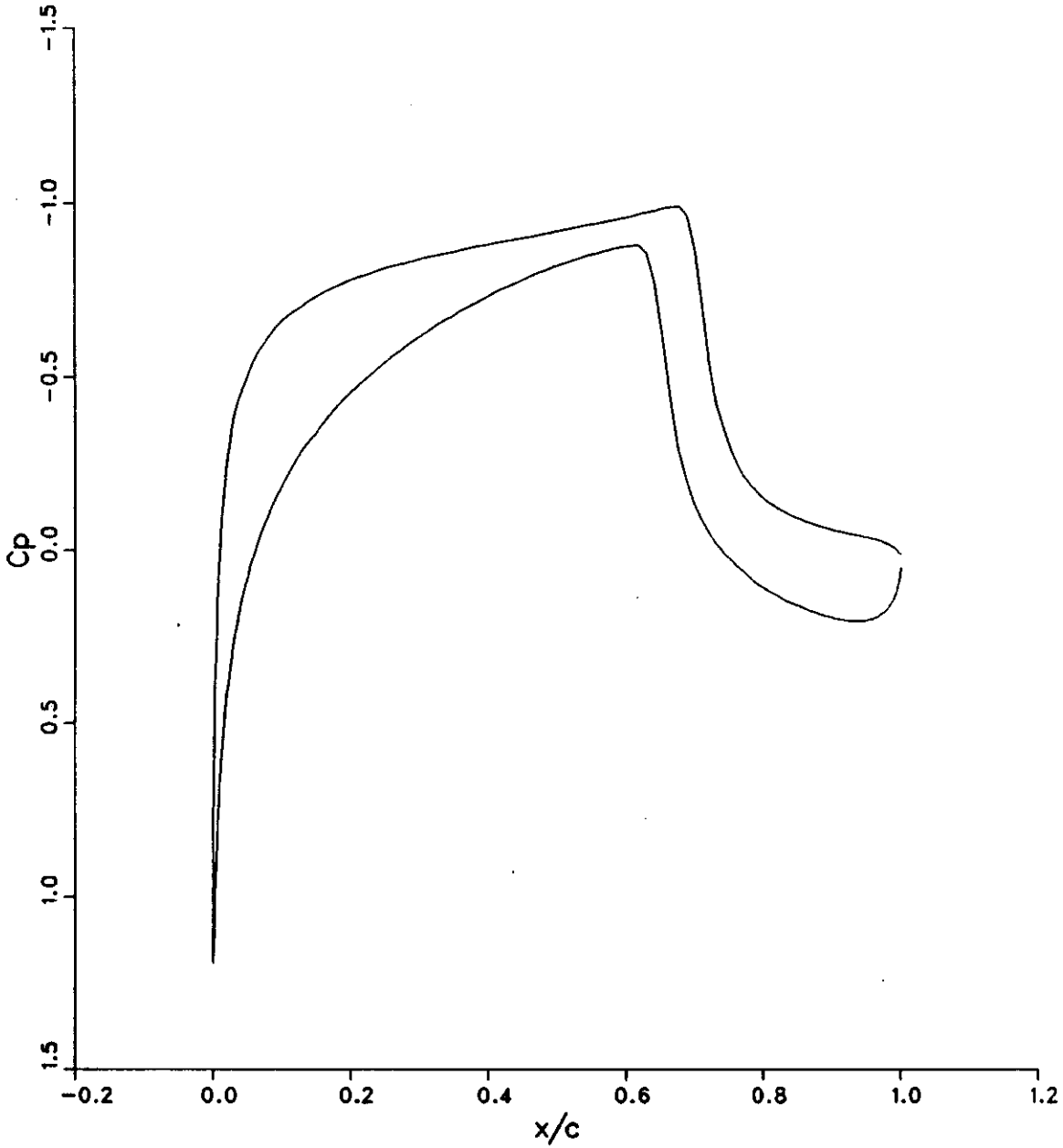

Figure 38 – Momentum thickness vs. x/c for case C10

JONES AIRFOIL

M = 0.85, alpha = 2.0

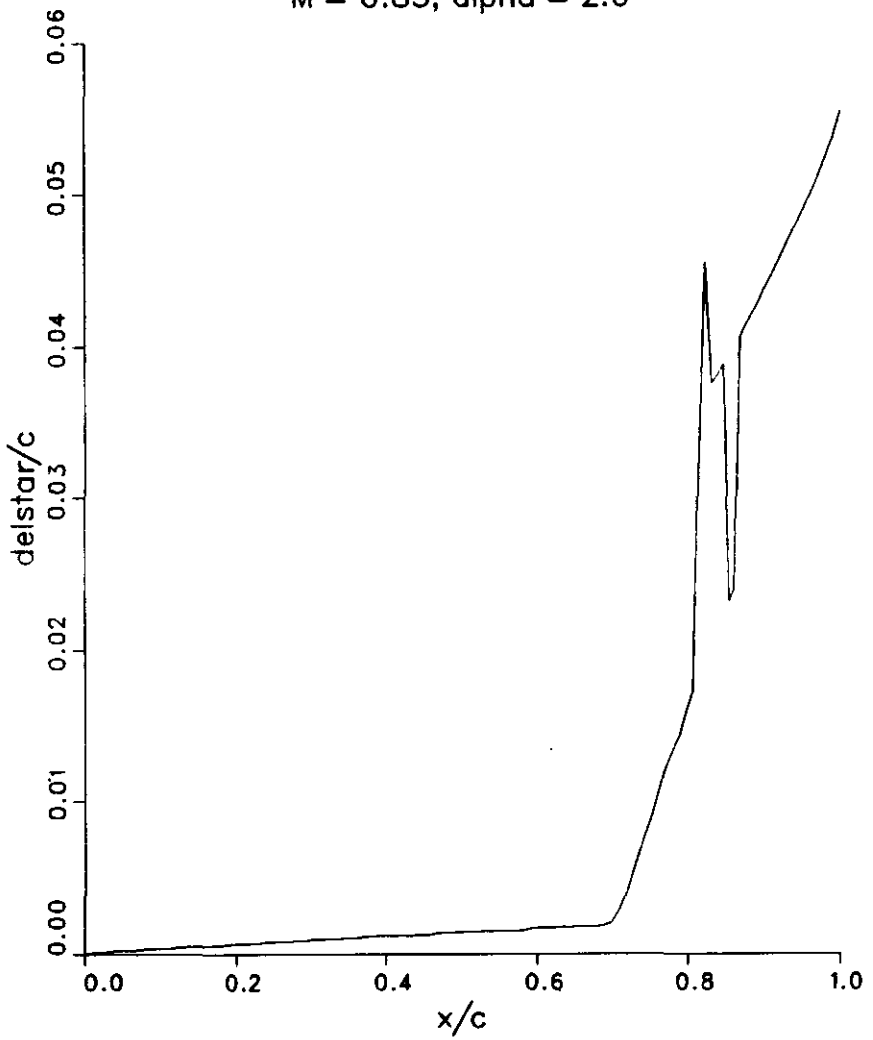

Figure 39 – Skin friction coefficient vs. x/c for case C11

JONES AIRFOIL

M = 0.85, alpha = 2.0

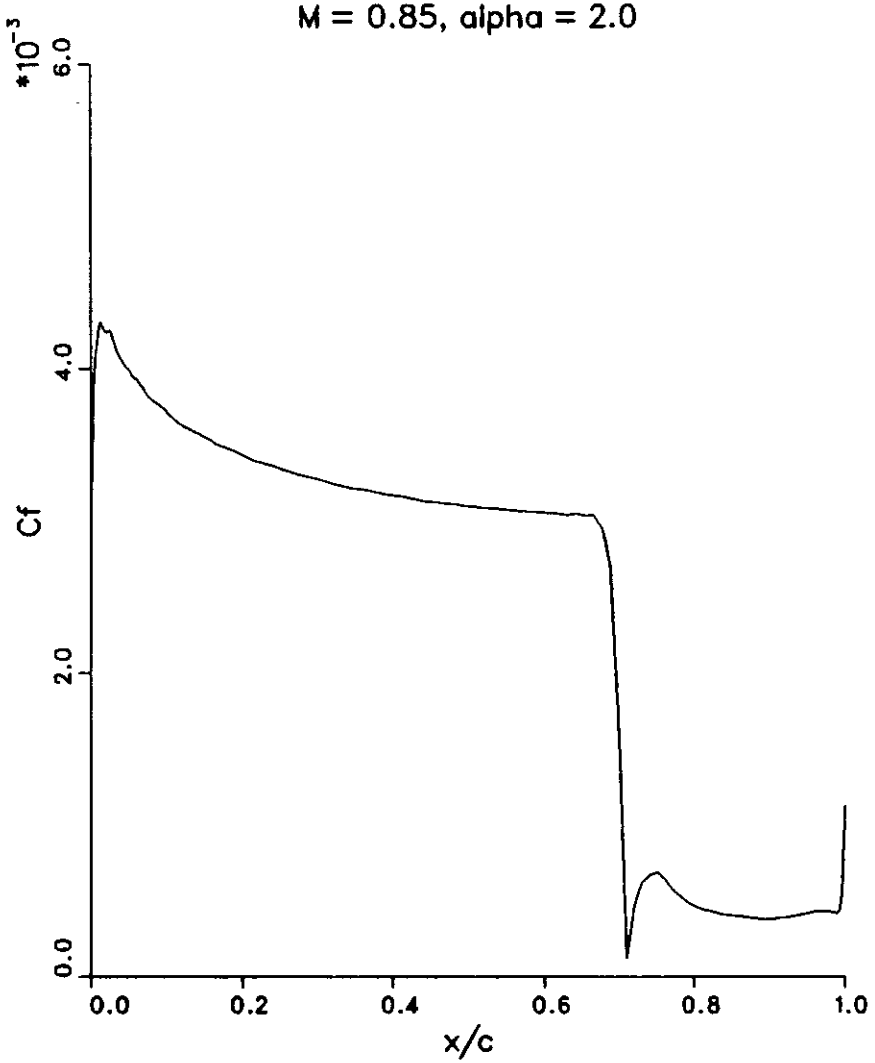

Figure 40a – Boundary layer profile at x/c = 0.6, case C12
JONES AIRFOIL
M = 0.85, alpha = 2.0

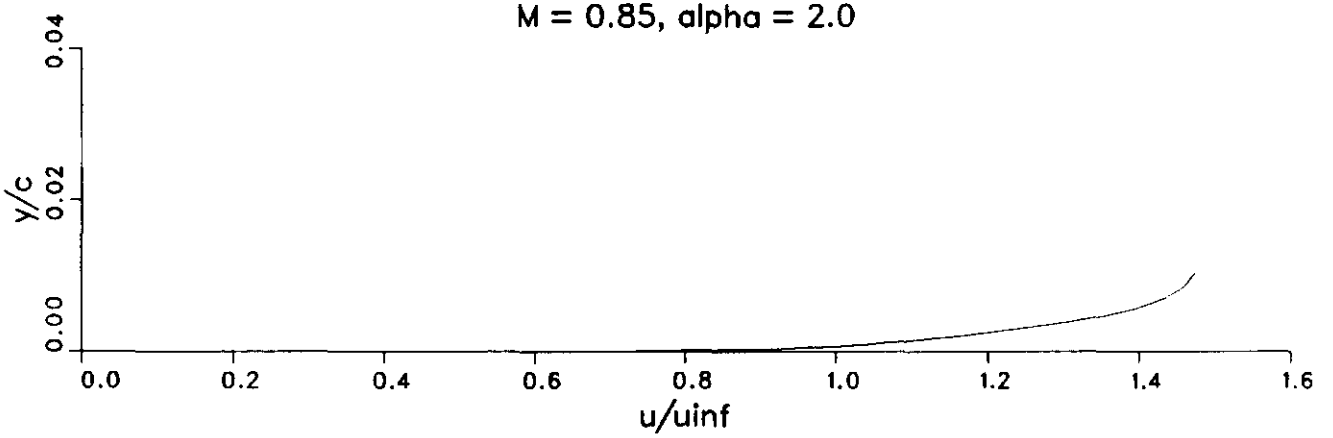

Figure 40b – Boundary layer profile at x/c = 0.6, case C12
JONES AIRFOIL
M = 0.85, alpha = 2.0

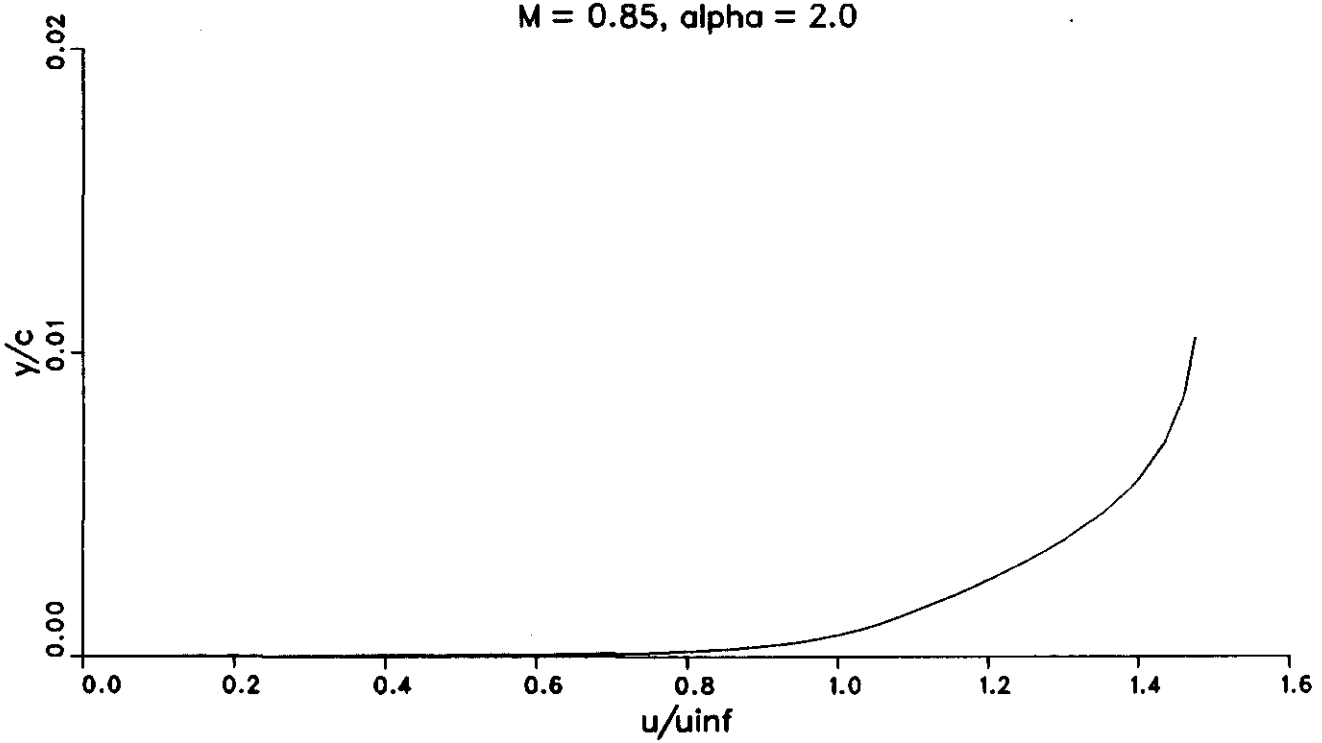
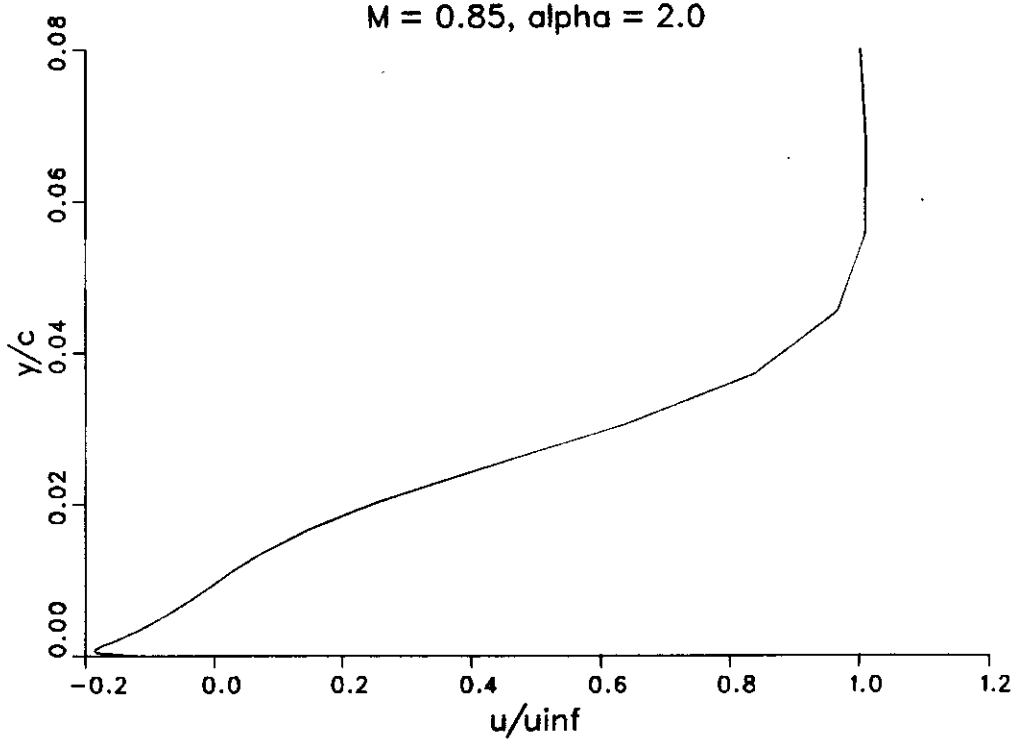
Figure 41 – Boundary layer profile at x/c = 0.9, case C13
JONES AIRFOIL
M = 0.85, alpha = 2.0